Current status of deMon2k for the investigation of the early stages of matter irradiation by time-dependent DFT approaches

Karwan Omar, Feven Korsaye, Rika Tandiana, Damien Tolu, Jean Deviers, Xiaojing Wu, Angela Parise, Aurelio Alvarez-Ibarra, Felix Moncada, Jesus Nain Pedroza-Montero, et al.

Current status of deMon2k for the investigation of the early stages of matter irradiation by time-dependent DFT approaches

Karwan A. Omar[1,2], Feven A. Korsaye[1,3], Rika Tandiana[1], Damien Tolu[1,4], Jean Deviers[1,5], Xiaojing Wu[6], Angela Parise[7], Aurelio Alvarez-Ibarra[1], Felix Moncada[8], Jesus Nain Pedroza-Montero[9], Daniel Mejia-Rodriguez[10], Nguyen-Thi Van-Oanh[1], Fabien Cailliez[1], Carine Clavaguéra[1], Karim Hasnaoui[11,12], Aurélien de la Lande[1*]

1) Université Paris Saclay, CNRS, Institut de Chimie Physique, UMR 8000, 91405, Orsay, France.

2) Department of Chemistry, College of Education, University of Sulaimani, 41005, Kurdistan, Iraq.

3) PSL University, CNRS, Chimie ParisTech-PSL, Institute of Chemistry for Life and Health Sciences (i-CLeHS), Theoretical Chemistry and Modelling Group (CTM), 75005 Paris, France.

4) CEA, DES, ISEC, DMRC, Université Montpellier, Marcoule, 30207 Bagnols-sur-cèze, France.

5) Department of Physics and Living Systems Institute, University of Exeter, Stocker Road, EX4 4QD Exeter, United Kingdom.

6) Department of Physics and Astronomy, University College London, London WC1E 6BT, United Kingdom.

7) Consiglio Nazionale delle ricerche/National Research Council (CNR)-IOM c/o International School for Advanced Studies (SISSA/ISAS), via Bonomea 265, 34136 Trieste, Italy.

8) Department of Physics, AlbaNova University Center, Stockholm University, S-106 91 Stockholm, Sweden

9) Institut Charles Gerhardt de Montpellier, CNRS, ENSCM, Université de Montpellier, 34296 Montpellier, France.

10) Environmental Molecular Sciences Laboratory, Pacific Northwest National Laboratory, Richland, WA 99352, USA

11) Institut du développement et des ressources en informatique scientifique, CNRS, UAR 851, bat. 506 BP 167 91403 ORSAY CEDEX – France

12) Maison de la Simulation, UAR 3441, Bâtiment 565 PC 190 – Digiteo CEA Saclay 91191 Gif-sur-Yvette cedex – France

To whom correspondence should be addressed: aurelien.de-la-lande@universite-paris-saclay.fr

Abstract

We summarize in this article the recent progress made in our laboratories in the development of numerical approaches dedicated to investigating ultrafast physicochemical responses of biological matter subjected to ionizing radiations. Our modules are integrated into the deMon2k software which is a readily available program with highly optimized algorithms for conducting Auxiliary-Density-

Functional-Theory (ADFT) calculations. We have developed a computational framework based on Real-Time Time-dependent ADFT to simulate the electronic responses of molecular systems to strong perturbations, while molecular dynamics simulations in the ground and excited states (Ehrenfest dynamics) are available to simulate irradiation-induced ultrafast bond breaking/formation. Constrained ADFT and Multicomponent ADFT have also been incorporated to simulate charge transfer processes and nuclear quantum effects, respectively. Finally, a coupling to polarizable force fields further permits to realistically account for the electrostatic effects that the systems' environment has on the perturbed electron density. The code runs on CPU or hybrid CPU/GPU architectures affording simulations of systems comprised of up to 1000 atoms at the DFT level with controlled numerical accuracy. We illustrate the applications of these methodologies by taking results from our recent articles that aimed principally at understanding experimental data from pulse radiolysis experiments.

List of Acronyms

ADFT : Auxiliary DFT
ADSIC : Average Density Self-Interaction Correction
BOMD : Born-Oppenheimer molecular dynamics
CAP : Complex Absorbing Potential
CT : Charge Transfer
DFT : Density Functional Theory
ELF : Electron Localization Function
EMD : Ehrenfest Molecular Dynamics
GGA : Generalized Gradient Approximation
ITP : Imaginary-Time-Propagation
KS : Kohn-Sham
LDA : Local Density Approximation
MC-DFT : Multi-Component DFT
MD : Molecular Dynamics
MO : Molecular Orbital
NBE : Non-Bonded-Electrons
PBE : Perdew, Burke and Ernzerhof
QM/MM : Quantum Mechanics / Molecular Mechanics
RT-TD-DFT : Real-Time TD-DFT
SCF : Self-Consistent-Field
TD : Time-Dependent
USP : Urinidine Sugar Phosphate
XC : Exchange-correlation
XUV : eXtreme Ultra-Violet

1 Introduction

The consequences of matter irradiation by high-energy particles is a topic of major interest in biology, medicine, physics, chemistry, or material sciences [1]. Fast ions (H^+, He^{2+}, ….) or other massive particles (μ^-, e^+, ….) with average kinetic energy falling in the range of a few tens of keV to a few MeV, as well as high energy photons (extreme UV, X, γ…) are ionizing radiations. They interact so strongly with the electron cloud of molecules that they cause high-energy electronic excitations, eventually expelling electrons toward the continuum. Ionizing radiations leaves matter with several electronic holes and a great amount of energy deposited within the electron cloud, not to mention the production of copious amounts of near-free electrons that further irradiate surrounding matter. A complex succession of physical, chemical, and eventually biological processes—spanning up to sixteen orders of magnitude in space and time—follows, finally leading to functional alterations of the irradiated systems. Irradiation damage of biological systems is a well-known example of radio-induced dysfunctions which, for example, are helpful to kill cancer cells (*i.e.* radiotherapies) [2,3]. Actually, the issues raised by ionizing radiations are important also in the nuclear industry, aeronautics, space industry, or for understanding astrochemistry. In all cases, the ultra-fast events taking place upon, and immediately after irradiation, are of the utmost importance as they condition all successive events.

It is customary to define the physical stage as the one covering the atto-to-femtosecond timescale (10^{-18}-10^{-15} s). Only the light electrons manifest appreciable motion within this timescale. The physical stage sees the deposition of energy into the electron cloud by the irradiating particle(s), inducing electronic excitations and, eventually, ionizations. In the latter situation, the photoelectrons (also known as secondary electrons) emitted to the continuum thermalize by collisions with surrounding matter and, eventually, excite other molecules. After the physical stage, the physicochemical stage (10^{-15}-10^{-12} s) witnesses complex non-adiabatic nuclear dynamics propelled by the energy deposited in the electron cloud. Energy is dissipated into vibrational modes, eventually leading to covalent bond cleavage. Subtle quantum effects involving electronic state crossings, interferences, coherence/decoherence, *etc*. are at play at this stage too. Secondary electrons lying in the continuum might get solvated or trapped in molecular cavities, typically in less than 1 ps in water [4,5]. They may also be captured in molecular resonant states, opening the door toward chemical bond breaking by dissociative electron attachment mechanisms [6]. Once the irradiated system has relaxed back to the ground electronic state, a rich chemistry is expected to expand over the nano-to-microsecond timescale depending on the reaction energy barriers to be overcome. This is usually referred to as the chemical stage of irradiation and has been extensively studied over the last decades, for instance, in the context of biological damages [7,8]. The biological stage refers to consequences happening in even longer timescales at the level of large

biological structures [9], DNA repair mechanisms [10], genome instability and epigenetic regulations [11,12] …

Focusing back on the ultrafast time scales, the first quarter of the XXI century has been particularly exciting due to the emergence of ultrafast spectroscopies and the advent of sophisticated numerical algorithms [13]. It is now possible to uncover the earliest mechanisms taking place after irradiation. High-harmonic generation and extreme free electron lasers provide extraordinary approaches to probe the responses of matter with attosecond resolution. For example, Loh *et al.* observed that proton transfer from an ionized water molecule to neighboring water takes place within a few tens of femtoseconds using tunable femtosecond soft x-ray pulses from an x-ray free electron laser [14]. Other examples are the observation of ultrafast charge migrations following ionization [13,15], or the formation of doubly ionized water by intra-coulomb decay in water. As often, the development of experimental techniques stimulates that of theoretical frameworks and of numerical simulation algorithms (e.g. [16–19]). The French theoretical community is also very active and develops diverse methodologies. Far from being exhaustive, and restricting here our attention to the short time scales, we mention Miteva, Sisourat, and co-workers who have developed a configuration interaction method to model Fano resonances with application to intra-coulomb decay processes [20]. Luppi and co-workers have explored the use of time-dependent configuration interaction for high-Harmonic generation spectroscopy calculations [21]. Other groups have developed dedicated theoretical frameworks to interpret attosecond experiments, including photoionization [22–25]. Semi-classical theoretical frameworks to deal with non-adiabatic dynamics are developed by Vacher [26,27], Agostini [28,29], Lasorne [30], Joubert-Doriol [31] and co-workers, while other groups develop fully quantum dynamical approaches such as the multiconfiguration time-dependent Hartree scheme [32,33], or dissipative quantum dynamics approaches [34,35]. Other groups in France have investigated by simulation the first stages of biological matter radiolysis [36,37] or even the longer consequences for large biostructures [38]. In this article, our objective is to review recent methodological developments carried out in our group at the Institute of Physical Chemistry to address the early stages involved in the radiolysis of biological matter by means of numerical simulations.

Our primary focus is to decipher the molecular mechanisms that lead to physicochemical damage on biological systems, although we occasionally explore other intriguing territories such as the chemical degradation of organic extractants of interest for the nuclear industry. We work in tight collaboration with experimental groups (atto- and femtosecond spectroscopists, radiation chemists, and biochemists). Having in mind the perspective of reaching more and more realistic descriptions of the simulated systems, we have decided to base our work on Density Functional Theory (DFT). DFT has emerged as a powerful quantum mechanical method in the second half of the XX century to investigate

the electronic structure of molecules and solids [39,40]. The extension of DFT to the time-dependent (TD) domain in the early 1980s has opened the door to the investigation of excited electronic structure and time-dependent phenomena [41,42]. In particular, Real-Time TD-DFT (RT-TD-DFT) permits the simulation of the responses of the electron cloud subject to strong, ionizing radiations [43–45]. In particular, it gives access in principle to the superposition of states produced by the irradiation. When coupled to the classical Newtonian dynamics of the atom nuclei ("ions" in physicists' language), it gives access to the physicochemical stages of matter radiolysis [37,46].

Within the overwhelming literature dedicated to (TD-)DFT developments [47,48], our objective has been modestly focused on new implementations of RT-TD-DFT, for dedicated applications to radiolysis simulations of nanometric, inhomogeneous systems such as those encountered in biology. Our objective is to devise, step-by-step, a set of integrated methodologies within a consistent simulation environment. In this article, we summarize these efforts and illustrate the kind of insights that becomes accessible to large-scale simulations. We mainly borrow illustrative examples from our previous publications, although some new results are presented too. We start our review by introducing the equations-of-motion to conduct electron dynamics simulations in the framework of Auxiliary DFT (ADFT), describing the main algorithms enabling simulations of large molecular systems. A multicomponent ADFT method to simulate proton transfers in electronic excited states with the inclusion of nuclear quantum effects, or electrons/positrons systems is then introduced. We then move on to the description of computational techniques to deal with the emission of electrons in the continuum. Notably, we detail the complex absorbing potentials available in our code to cope with these phenomena. We dedicate a section to issues arising from the approximations of exchange-correlation functionals available in our code. Regarding the problem of electronic self-interaction error, we report a time-dependent descriptor designed to chase spurious charge transfer dynamics in RT-TD-DFT simulations. We then introduce the topological analyses of the time-dependent electron localization function. In the last sections, we describe, on one hand, the coupling of (TD-)ADFT to molecular dynamics in the ground or excited electronic states and, on the other hand, the coupling of RT-TD-DFT to polarizable molecular mechanics. We review a few examples of applications we have published recently using these methodologies.

2 Electron dynamics simulations

When a high-energy photon or a particle irradiates matter, the interaction takes place at the level of the electron cloud. A methodology giving access to the dynamics of electrons on the attosecond time scale is therefore mandatory to properly capture the physics at play. On this time scale, atom nuclei can be regarded as static, and in the so-called pure RT-TD-DFT approach, only electronic motion is propagated in time. In this first section, we introduce the basic equations-of-motion for electron

dynamics simulations together with the kind of irradiation amenable to simulation with our code. All our implementations have been carried out in the framework of the deMon2k program [49], which is a readily available program for academic groups. deMon2k is specialized in the realization of stationary electronic structure calculations, in the calculation of response properties by perturbative approaches, and in first-principles molecular dynamics. Instead of devising an RT-TD-DFT program from scratch, we considered it more appealing to build on an already existing and highly optimized code. Unless otherwise stated, we will use Hartree atomic units throughout the article. Vectors will be written with bold characters.

2.1 Real-time propagation of electron densities

The foundations of DFT for stationary electronic structure calculations were exposed in the seminal article of Hohenberg and Kohn [39]. There, it was proven the existence of a one-to-one mapping between the electron density and the external potential, up to a constant potential value. In principle, the electronic energy can be obtained as a functional of the electron density, comprising the electronic kinetic energy, the electron-electron interaction, and the potential energy arising from the interaction of the electron density with an external potential. Later, Kohn and Sham proposed to invoke an auxiliary (reference) non-interacting electron gas that has the same density as the real system [40]. In this approach, the total electronic energy is the sum of the kinetic energy of the non-interacting electron gas, of the classical Coulomb repulsion between electrons, of their interaction with the external potential (v_{ext}), and an exchange-correlation (XC) energy that collects all the interacting quantum effects related to the quantum nature of the electrons. The external potential includes that created by atom nuclei of the quantum system and eventually by the environment (see below).

The extension of DFT to time-dependent external potentials is due to Runge and Gross [41]. These authors showed that there is a unique mapping between the time-dependent external potential (up to a constant) of a system and its time-dependent density provided that an initial wave function is known. The TD-DFT equations may be expressed with a Liouville-von Neumann equation [50,51].

$$i\frac{\partial \rho(r,t)}{\partial t} = [H(r,t), \rho(r,t)] \qquad (1)$$

in which ρ is the electron density and H is the electronic Hamiltonian. Within the Kohn-Sham (KS) framework, ρ is built from the so-called KS molecular orbitals (MO):

$$\rho(r,t) = \sum_i \psi_i^*(r,t)\psi_i(r,t) \qquad (2)$$

where the sum index i runs over all electrons of the system. The full electronic Hamiltonian can therefore be written as:

$$H(t) = -\sum_i \frac{1}{2}\nabla_i^2 + \int \frac{\rho(r',t)}{|r-r'|}dr' + v_{XC}[\rho(r,t)] + v_{ext}(r,t) \quad (3)$$

The second term on the r.h.s., v_{XC}, v_{ext} are respectively the electronic Coulomb repulsion potential, the exchange-correlation potential and the external potential, the sum of which defines the so-called Kohn-Sham potential v_{KS}. External perturbations such as the electric field generated by laser fields or by fast-moving ions are other contributors to v_{ext}. The types of perturbations available in deMon2k will be described in a following section. The numerical propagation of Eq. (1) faces the issue that H, being a functional of the density, is intrinsically time dependent. Propagation over long time scales (*e.g.* for tens of attoseconds) is therefore not possible. In practice, we achieve propagation by discretizing the time variable into small time steps Δt_e of the order of 0.1-5 as. The propagator should fulfill two important properties: it has to be unitary and time-reversible [48,52]. In deMon2k we currently have implemented the second-order Magnus method [48,53].

$$\rho(t_n + \Delta t_e) = e^{-iH\left(t+\frac{\Delta t_e}{2}\right)*\Delta t}\rho(t_n)e^{iH^*\left(t+\frac{\Delta t_e}{2}\right)*\Delta t} \quad (4)$$

Eq. (4) propagates the electron density from t_n to $t_n + \Delta t_e$, knowing the Kohn-Sham potential at time $t_n + \frac{\Delta t}{2}$. Two propagation schemes, relying either on an iterative [52] or on a predictor-corrector [54] (PC) solvers, are available in deMon2k. The iterative solver is the most robust and, provided a sufficiently small time step, almost always ensures a stable propagation [48]. The PC solver turned out, in our experience, to be also stable in most simulations if it is used with time steps of the order of 1 as. As the PC solver needs only one evaluation of the KS potential per propagation step, it allows large computational time savings. A demanding task is the evaluation of the exponential of the KS matrix. In deMon2k, the user has the choice between a straightforward diagonalization of the matrix, a Taylor expansion, a Chebyshev expansion, or a Baker–Campbell–Haussdorff [51] expansion to operate this task [52].

2.2 Imaginary time propagation of electron densities

Before conducting RT-TD-DFT propagation, it is necessary to obtain the electronic ground state density of the system. This can be done by solving the stationary Kohn-Sham equations [55]. Each orbital ψ_i is the solution of an eigenvalue equation, $\left(-\frac{1}{2}\nabla_i^2 + v_{KS}\right)\psi_i = \varepsilon_i\psi_i$, involving the KS potential v_{KS}. These eigenvalue equations are highly nonlinear because the KS potential is itself a functional of the electron density. As with most quantum chemistry codes, deMon2k solves the set of homogeneous KS equations via a self-consistent-field procedure (SCF) involving the diagonalization of the KS

Hamiltonian[1]. Imaginary time propagation (ITP) is an alternative to obtain the electronic ground state [57]. ITP has been made available in deMon2k as part of this work. ITP is an approach based on the Wick rotation of time, from t to $-it$, in Eq. (3). This leads to the propagator $U(t+\Delta t) = e^{H\left(t+\frac{\Delta t_e}{2}\right)*\Delta t}$. Therefore, starting from a trial wavefunction $|\Psi(0)\rangle$ decomposed over the eigenstates $|\phi_i\rangle$ with amplitudes $A_i(0)$, ITP leads to a wave function $|\Psi(\tau)\rangle = \sum_{i=0}^{\infty} A_i(0)e^{-\tau E_i}|\phi_i\rangle$ after a propagation time τ. Because of the exponential term, it is apparent that the system accumulates ground state character over time.

ITP may have advantages over SCF in cases where SCF convergence is tedious to obtain, for example in systems with highly degenerate electronic structures like transition metal complexes with partially filled *d,* or in lanthanides with partially filled 4*f* orbitals. For instance, Flamant *et al.* reported ITP simulations for Cu_{15} and Ru_{55} nanoclusters [58]. The implementation in periodic DFT systems reported by McFarland *et al.* [59] and Hekele *et al.* [60] evidenced that the ITP framework allows to reach ground state energy of metallic systems, usually difficult to achieve with conventional SCF iterations. In addition to SCF convergence issues, the diagonalization step involved at each SCF cycle may also become computationally expensive for large systems and can be handled more easily by ITP. ITP also permits to find electronic ground states in the presence of complex absorbing potentials, a feature that proves useful when trying to identify resonant states.

2.3 Ground state density perturbation, first applications

An electronic propagation is generally launched from the ground state density on which an external perturbation is applied. deMon2k currently implements several kinds of perturbations opening the door toward the simulation of several physicochemical phenomena of interest. Our code can cope with irradiation with XUV (eXtreme Ultra-Violet) photons (or lower energy photons) and with light fast ions (*e.g.* H^+, He^{2+}…). Irradiation with higher energy photons (X-, γ-rays), heavy ions (*e.g.* Ni^{22+}, …), or with another kind of quantum particles (*e.g.* μ^-) are left for future work.

For photon irradiation, we adopt the electronic dipole approximation. The electric field component ($\boldsymbol{F}_e$) of the electromagnetic wave interacts with the dipole moment of the molecule ($\boldsymbol{\mu}$): $E^{pert}(t) = -\boldsymbol{\mu}(t) \cdot \boldsymbol{F}_e(t)$. $\boldsymbol{F}_e$ may be modeled as the product of a monochromatic light electric field and a carrier function (*i.e.* a Gaussian pulse, a squared sinusoidal pulse or a linear ramp). Although not yet implemented, a succession of pulses is also straightforward to implement and would be useful to

[1] To mitigate this last statement though, we indicate that a diagonalization-free SCF solver has been recently developed by Köster and co-workers in deMon2k [56].

simulate pump-probe experiments. $\boldsymbol{F}_e$ may alternatively be an instantaneous electric kick, which is useful for simulating the absorption spectra of a molecule. Indeed, the line shape of the absorption spectrum of a molecule can be estimated from the dipole strength function S that is related to the absorption cross-section tensor σ expressed in the frequency domain: $S(\omega) = \frac{1}{3} Tr[\sigma(\omega)]$. σ is evaluated from the imaginary part of the complex polarizability tensor α, *i.e.* $\sigma = \frac{4\pi\omega}{c} \mathrm{Im}[\alpha(\omega)]$, with c being the speed of light. Therefore, an absorption spectrum can be evaluated using RT-TD-DFT launching three individual electron dynamics simulations from a stationary electron density and perturbed by a weak electric field of strength κ applied along either the *x*, *y* or *z* directions (d). The Fourier transform of the dipole moment (μ_j) recorded along the simulation gives access to the polarizability tensor α: $\alpha_{d,j} = \frac{1}{\kappa} \mu_{d,j}(\omega)$ [61]. Eventually, one may simplify the procedure and run a unique simulation with the field aligned in the x, y *and* z directions at a time. As an illustrative example, Figure 1 depicts the absorption spectra of gold nanoparticles, that we have calculated for this article with one RT-TD-ADFT simulation for each field direction. The spectra reveal a red-shift of the lowest-energy absorption peak when increasing the nanoparticle size.

Excitations caused by fast ions are achieved via Coulomb scattering. The interaction energy for a projectile holding an electric charge q_{proj} and traveling with speed v_{proj} is best described with a Liénard-Wiechert potential [62]: $E^{pert}(t) = \int_{space} \gamma \rho(r) q_{proj} / R \, dr$ with γ being the angle-dependent Lorentz factor $\left(1 - v_{proj}^2 (sin\Theta)^2 / c^2\right)^{-1/2}$. In these last expressions, R is the distance between an electron and the projectile, and Θ is the angle formed between the projectile propagation line and electron-projectile axis. For projectiles traveling at speeds much smaller than c, the Liénard-Wiechert reduces to a standard Coulomb potential ($\gamma \to 1$).

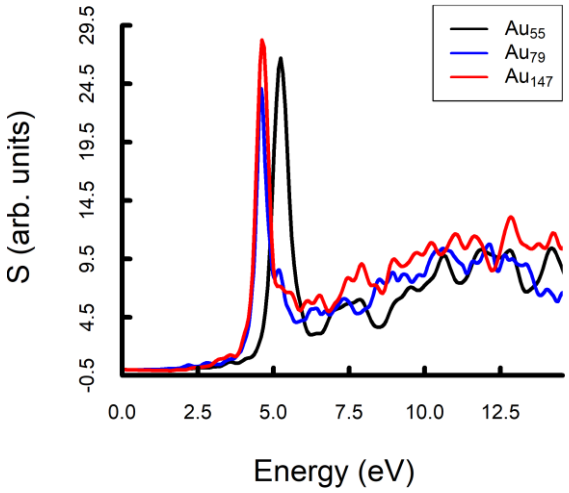

Figure 1: absorption spectra of gold nanoparticles of different sizes obtained by RT-TD-DFT simulations with deMon2k. After ITP a Dirac electronic kick of strength 0.06 a.u. was applied. RT-TD-ADFT propagations were pursued for 9 fs with a 0.001 fs time step. PBE XC functional [63] and relativistic core potentials with associated basis set have been used [64].

Finally, an alternative method to the application of an external perturbation to the ground state density is to manually modify the occupation numbers of the ground state MOs so as to create a fictitious starting electronic state. We may either conduct a separate Casida's TD-DFT calculation [42] to prepare a desired excited state or hole(s) can be created in the electronic structure ("sudden ionization approximation"). Figure 2 compares the charge migrations taking place after the ionization of an uridine monophosphate molecule, around the sugar moiety, caused either by a collision with an α-particle or by depopulation of a MO localized in the sugar (after applying a Pipek-Mezey MO localization procedure [65]). Both approaches indicate that the hole initially created on the sugar part delocalizes on the nucleobase after a few fs, while the phosphate group does not accumulate charge over the simulation. On the other hand, we see noticeable differences between the two graphs. The charge on the nucleobase is higher 3 fs after ionization with the sudden ionization approximation . The charge on the water solvation shell is largely negative when we simulate collision indicating the localization sites of the electrons expelled from the sugar. In fact, with the sudden ionization approximation an electron is completely removed from the system, thus the water shell's charge remains rather small. We refer the reader to [66] for a deeper analysis of these results.

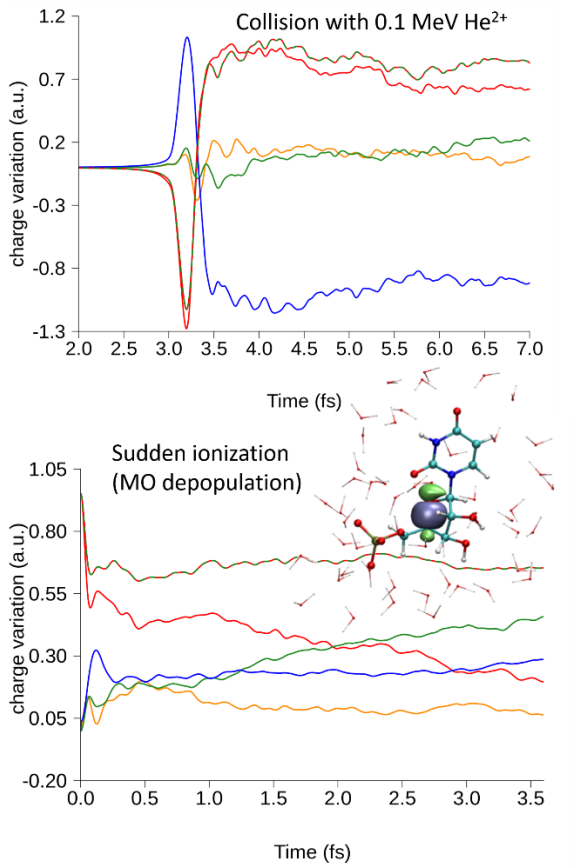

Figure 2: charge migrations following ionization a uridine monophosphate molecule solvated in water at the level of the sugar moieties. The hole on the sugar group is created either upon collision with an α-particle at 3.2 fs (top) or by depopulation of MO localized on the sugar (bottom) at time 0. The curve represents Hirshfeld [67] charge variations with respect to the ground state. Color code: sugar in red, nucleobase in green, phosphate group in yellow and solvation shell in blue, sugar+nucleobase in red-green. Adapted with permission from [66].

2.4 Electronic propagations with Auxiliary DFT potentials

We describe in this section some practical details of our implementation within the so-called Auxiliary Density Functional Theory framework. First, we expand the Kohn-Sham molecular orbitals as linear combinations of atomic orbitals:

$$\psi_i(r) = \sum_{\mu} c_{\mu i}\, \mu(r) \qquad (5)$$

where μ represents a basis function and $c_{\mu i}$, are the complex molecular orbital coefficients. We use Gaussian-type functions as basis sets. This methodological choice raises caution points regarding the ability to describe certain processes induced by strong perturbation of the density, such as ionization. A section will be dedicated to this point below. The reason for choosing Gaussian functions is the availability of highly performant algorithms developed by the quantum chemistry community to calculate electronic integrals [68,69]. The Kohn-Sham energy expression for the system in the presence of an external perturbation reads:

$$E = \sum_{\mu,\nu} P_{\mu\nu}\, H_{\mu\nu}^{core} + \frac{1}{2}\sum_{\mu,\nu}\sum_{\sigma,\tau} P_{\mu\nu}\, H_{\mu\nu}\langle\mu\nu||\sigma\tau\rangle + E_{xc}[\rho] + E_{pert}[\rho] \quad (6)$$

where the $P_{\mu\nu}$ is the density matrix defined as:

$$P_{\mu\nu} = 2\sum_{i}^{occ} c_{\mu i}^{*} c_{\nu i}, \quad (7)$$

and $H_{\mu\nu}^{core}$ are elements of the core Hamiltonian for one-electron interactions. The double vertical bar ($||$) denotes the Coulomb operator. Although our code deals either with closed- or open-shell electronic structures, we will be focusing on the former case here, for the sake of simplicity. The classical electron-electron repulsion (second term on the r.h.s. of Eq. (6)) represents a computational bottleneck. If solved, a second bottleneck comes from the evaluation of the XC contribution (E_{xc}). To overcome these issues, deMon2k implements the ADFT framework [70]. ADFT relies on the variational fitting of the Coulomb potential, which approximates four-center-electron-repulsion-integrals (ERIs) by two- and three-center integrals [70–72]. To this end, an auxiliary density function ($\tilde{\rho}$), expressed as a linear combination of auxiliary basis functions ($\tilde{\rho}(r) = \sum_{\bar{k}} x_{\bar{k}}\bar{k}(r)$), is fitted to reproduce as closely as possible the Coulomb repulsion energy. The procedure is variational and leads to the following energy:

$$E^{ADFT} = \sum_{\mu,\nu} P_{\mu\nu}\, H_{\mu\nu}^{core} + \sum_{\mu,\nu}\sum_{\bar{k}} P_{\mu\nu}\langle\mu\nu||\bar{k}\rangle x_{\bar{k}} - \frac{1}{2}\sum_{\bar{k},\bar{l}} x_{\bar{k}}\,\langle\bar{k}||\bar{l}\rangle x_{\bar{l}} + E_{xc}[\tilde{\rho}] + E_{pert}[\rho] \quad (8)$$

Note that the auxiliary density enters the exchange-correlation contribution (XC) too. deMon2k is equipped with an algorithm to automatically generate auxiliary function sets ($\{\bar{k}\}$) from a given atomic orbital basis set. For the sake of computational efficiency, the auxiliary basis set functions are atom-centered primitive Hermite-Gaussian functions grouped in sets sharing the same exponent [73]. Importantly, ADFT is variational and the error made by introducing the fitted density can be systematically reduced by augmenting the quality of the auxiliary basis set. The matrix elements of the Kohn-Sham potential derived from the ADFT energy expression reads:

$$K_{\mu\nu} = \left(\frac{\partial E^{ADFT}}{\partial P_{\mu\nu}}\right) = H_{\mu\nu}^{core} + \sum_{\bar{k}}\langle\mu\nu\|\bar{k}\rangle\left(x_{\bar{k}} + z_{\bar{k}}\right) + \left(\frac{\partial E_{pert}[\rho]}{\partial P_{\mu\nu}}\right) \quad (9)$$

$$z_{\bar{k}} = \sum_{\bar{l}}\langle\bar{k}\|\bar{l}\rangle^{-1}\langle\bar{l}|v_{xc}\rangle \quad (10)$$

$v_{xc} \equiv \partial E_{xc}/\partial\tilde{\rho}$ is the exchange-correlation potential. The KS potential does not explicitly depend on the orbital density, but only on the fitted density, hence the ADFT denomination [74]. To investigate ionization processes or electronic transport, it may be useful to add complex absorbing potentials

(CAP) to the KS potential. This approach will be detailed in section 3.1. Actually, depending on the sign of the CAP, electrons can be removed from or injected into the system during RT-TD-ADFT simulations. All integrals, except those involving XC contributions or CAP (when defined in the real space, see below), are evaluated by analytical methods, providing almost machine precision (16 decimals). The other integrals are evaluated by numerical integration over atom-centered Lebedev grids [75]. Tabulated grids or adaptive grids [75] with user-defined accuracy are available to carry out this task.

deMon2k implements a wide range of models to evaluate XC contributions and is interfaced with the LibXC library [76]. The choice of functionals available includes Local Density Approximation (LDA), generalized gradient approximation, or meta-generalized-gradient-approximation functionals. Global hybrids and range-separated hybrids that incorporate constant or distance-dependent Fock potential contributions are also available for RT-TD-ADFT simulations. In the latter case, a variational fitting of the Fock potential is introduced to avoid four-centers-integrals and reduce computational cost. Importantly this algorithm is coupled to a localization procedure that permits the screening of integrals that do not contribute to the Fock potential (see References [77,78] for details). So far, all functionals available in deMon2k to conduct RT-TD-ADFT simulations ignore memory effects in the XC potential (adiabatic approximation). This point will be discussed in depth in section 3.2.

In summary, the ADFT methodology from deMon2k allows a drastic reduction of the computational cost and the scaling law with system size, with controllable accuracy, as compared to a "naïve" implementation of KS-DFT. We have adapted this technology to RT-TD-ADFT thereby enabling electron dynamics simulations within large systems. We extensively assessed the reliability of RT-TD-ADFT for the calculation of absorption spectra, electronic stopping power, or attosecond charge migrations, and found that ADFT is a reliable methodology [79].

2.5 High-Performance Computing

We have dedicated substantial efforts to improving the computational performance of our RT-TD-ADFT module. Currently, systems with up to 1,000 atoms can be handled in routine simulations or, said alternatively, systems containing a few thousands electrons [61,80]. Effective core potentials and model core potentials [81] are available to remove core electrons from the list of explicitly represented particles and to reduce computational timing. Figure 3, left, is an example of the benchmarks we have published in the last years for a series of water clusters ranging from 50 to 500 molecules [19,61,79]. Obviously, the cost associated with the calculation of the Kohn-Sham potential is manageable even for the largest droplet (5,000 electrons) and exhibits a favorable scaling law. This result indicates that our RT-TD-ADFT module fully benefits from the algorithmic machinery developed by Köster and co-workers for stationary calculations, notably, the MINRES approach [82] to density fitting and the double

asymptotic expansions schemes [83,84] to handle electronic integrals calculations. The most demanding computational task in RT-TD-ADFT is the calculation of the propagator ("matrix exponentiation"), Eq. 4. It is evaluated here using a Taylor series with an interface with the ScaLAPACK library [85] which shows good parallelization properties [19,61]. In the case depicted in Figure 3, one could use up to 400 CPUs with appreciable gain and to further strongly decrease the cost of the simulation [19]. To go one step beyond in terms of efficiency, we have recently developed a hybrid CPU/GPU code with very encouraging results [86]. In our current implementation, matrix exponentiation and basis transformations are handled by GPUs. The graph on the right-hand side attests to the drastic decrease in the computational cost now associated with these tasks, showing a reduction by a factor of almost 40 for the largest droplet containing 500 molecules. There is actually still room for further improvement of code performance.

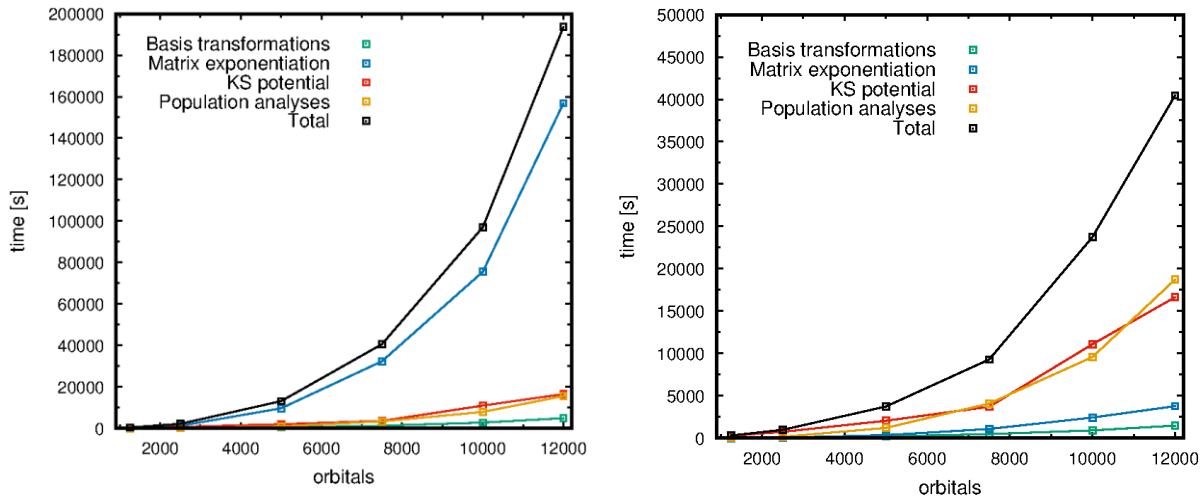

Figure 3: large water droplets containing up to 5,000 electrons are amenable to RT-TD-ADFT simulations (version 6.1.6). Timings to conduct 1 fs simulations with a time step of 50 as, PBE functional with a direct scheme to calculate electronic repulsion integrals. The x-axis represents the number of atomic orbitals. Calculations run on the Jean Zay supercomputer (at IDRIS) on 2 Intel Cascade Lake 6248 processors (20 cores at 2.5 GHz), namely 40 cores per node, 192 GB of RAM memory and 4 Nvidia Tesla V100 16GB GPU cards. Left: Pure CPU simulations conducted with ScaLAPACK (40 CPU cores). Right: hybrid CPU-GPU simulations (40 CPUs and 4 GPUs used). Note the change of scale between the two graphs. Adapted with permission from [79] and [86].

2.6 Real-Time Time-Dependent Multicomponent ADFT

Multicomponent DFT (MC-DFT) provides a theoretical framework to describe quantum mechanical systems composed of particles with different masses, charges, or spins. MC-DFT is rooted in an extension of the Hohenberg-Kohn theorems for composite systems where the total energy is a functional of the one-particle densities, which are built from reference non-interacting orbitals under the Kohn-Sham formalism [87]. MC-DFT has been employed to incorporate nuclear quantum effects beyond the Born-Oppenheimer approximation [88–90] and to analyze the interaction of atoms and molecules with exotic particles such as positrons [91] and muons [92]. The MC-DFT approach provides a more efficient framework for the inclusion of quantum effects as compared to traditional path

integral methods [93]. Moreover, time-dependent (TD) MC-DFT methodologies have been formulated based on an extended Runge-Gross theorem for multicomponent quantum systems [94]. Linear response TD-MC-DFT has been employed to simultaneously compute the vibrational and electronic absorption spectra of small molecules [95,96]. Those spectra have also been computed from real-time (RT) propagation of the electronic and nuclear densities [97]. In addition, RT-TD-MC-DFT propagation has been used to study the dynamics of a positronic molecule in a laser field [98]. Furthermore, the RT-TD-MC-DFT method has been coupled with Ehrenfest dynamics to study excited-state proton transfer reactions [99]. In this approach, the transferred proton and the electron propagations are described with RT-TD-MC-DFT while the remaining nuclei move classically [97].

It is important to note, however, that despite many advances in the field, the development of quantum-particle-electron correlation functionals is still a major challenge that hinders the widespread adoption of MC-DFT methods.

Recently, we extended the Auxiliary DFT (ADFT) formulation to multicomponent systems [100,101]. In the current deMon2k code, auxiliary densities can be safely used to evaluate the electron-electron, proton-proton, and electron-proton Coulomb interactions, along with the electron-proton correlation energy [101]. A few LDA functionals have been implemented to evaluate the latter contribution [88–90]. Including the ADFT formalism in the MC-DFT framework significantly decreases the computational effort, as it reduces the formal scaling of the MC-DFT calculations with respect to the number of electrons and protons [101]. The real-time propagation of the auxiliary density for multicomponent systems has also been proposed. The implementation of this RT-TD-MC-ADFT method is currently underway and will be described in due course.

3. Matter under strong perturbations

3.1 Complex absorbing potential, Gaussian basis sets and all that

RT-TD-ADFT simulations give access to response properties of molecules subjected to weak or strong perturbations. Above and near ionization transitions raise several issues related to the description of continuum states (non-bonded electrons, NBEs). These transitions are characterized by resonance states that quickly decay, eventually through auto-ionization channels [102]. Furthermore, because of the localized basis set used in deMon2k, the continuum turns out to be represented as a succession of discrete electronic states [21]. This leads to artificially higher ionization transitions than expected. These transitions also create spurious absorption bands at high energy spectra that further can contribute to unreal auto-ionization events. NBEs, on the other hand, are reflected back to the molecular system when they reach the border of the space spanned by the chosen basis set, while in

reality, NBEs would escape the system. In the presence of a laser field, NBEs are driven back to the bath of bound electrons, therefore perturbing the "real" electron dynamics taking place there. NBEs finally pose technical issues when trying to define atomic charges and charge flows when analyzing the outputs of the simulations.

To cope with the artificial confinement of NBEs, a common approach is to introduce a complex absorbing potential (CAP) that removes fractions of electrons in the course of the simulation. As their name indicates, CAPs are introduced in the imaginary part of the Kohn-Sham potential (Eqs. 3 and 9). Two flavors of CAP are available in deMon2k. In the first one, the potential is defined according to distance criteria in the real space ("spatial CAP") [102], while in the other it is defined according to the energies of the Kohn Sham MOs describing NBEs. As in the work of Schlegel and co-workers, the former is built from a superposition of atom-centered CAPs (v_a^{space})[103].

$$v^{space}(r) = min_a \sum_{a=1}^{Natoms} v_a^{space}(r) \tag{11}$$

$$v_a^{space}(r) = \begin{cases} 0, r \leq R^\circ \\ V^{max} sin^2\left[\frac{\pi}{2W}(r - R^\circ)\right], R^\circ < r < R^\circ + W \\ V^{max}, r \geq R^\circ + W \end{cases} \tag{12}$$

The CAP strength smoothly increases beyond a threshold distance from the molecule (R°) and reaches a maximum value (V^{max}), when the distance reaches $R^\circ + W$. In our code, spatial CAPs are calculated by numerical integration of atom-centered Lebedev grids, with a user-defined accuracy. The parameters R°, W and V^{max} have to be carefully optimized, for example, by running a perturbation-free RT-TD-ADFT simulation from the SCF solution and by checking energy and wavefunction's norm conservations. A spatial CAP positioned too close to the molecule would absorb bound electrons in the ground state, which is generally not the desired outcome. Spatial CAPs are tricky to use with localized basis sets. First, basis functions need to be present to describe electrons at large distances, using very diffuse functions and/or grids of ghost atoms [103]. This causes an increase of computational cost due to the increase of the number of basis functions and of the grid points necessary to evaluate XC integrals, not to mention the risk of linear dependences within the basis set. Second, spatial CAPs do not distinguish unbound electrons from bound electrons in very diffuse states (*e.g.* Rydberg states). As a consequence, a spatial CAP will not absorb the sole NBE, making the interpretation of results delicate sometimes. Ideally one would position a spatial CAP far away from the molecule (*e.g.* by setting $R^\circ > 50$ Å), but this would be associated to an explosion of the computational cost with a code relying on localized basis sets.

An alternative is to define CAP based on another property of NBEs, namely their energies. We may indeed decide to absorb electrons populating MOs of high energy in the course of RT-TD-ADFT simulations. Lopata and coworkers used this method to simulate near-edge X-ray absorption spectra [104]. Energy CAP can be defined as follow:

$$v^{ener} = C'(t)\Gamma C'^{*(t)} \quad (13)$$

$$\gamma_i = \begin{cases} 0, \dot{\varepsilon}_i \leq 0, \\ \gamma_0[exp(\xi\dot{\varepsilon}_i) - 1], \dot{\varepsilon}_i > 0. \end{cases} \quad (14)$$

C' is the matrix of the MO coefficients in an orthonormal basis [105] and Γ is a diagonal matrix, the non-zero elements of which are defined by Eq. 14. γ_i can be interpreted as an ionization rate of an electron in state i associated to a lifetime $1/2\gamma_i$. Three empirical parameters define this lifetime, namely γ_0, ξ and ε_O. γ_0 has units of energy and sets the energy scale. ξ specifies the speed at which electrons populating state *i* will be absorbed. It has units of reciprocal energy. The higher the Kohn-Sham state the smaller the lifetime. ε_O is the vacuum energy cut-off introduced to shift the ith MO level $\dot{\varepsilon}_i = \varepsilon_i - \varepsilon_O$. This shift is needed to account for the underestimation of the ionization potential with almost all XC functionals (see the dedicated section 3.2). It is thus strongly dependent on the functional. As the energy of the lowest unoccupied MO (ε_{LUMO}) equals the opposite of electron affinity for the exact functional [106], one can set ε_O to enforce this equality provided separate calculations are done to evaluate the electron affinity of the system of interest. Alternatively, one can use Casida's formulation of TD-DFT to estimate ε_O [104]. In general, ε_O is thus also system dependent

For weak perturbations, the energy CAP may be evaluated only once from the SCF solution (see *e.g.* [104]). On the other hand, for stronger perturbations associated with significant electron density absorption the electronic spectrum varies (ε_i) and one should re-evaluate the CAP on-the-fly. This is not an option we have explored so far. At present, our experience with CAP defined by Eq. 11-14 is mitigated because of the sensitivity of the results obtained with the chosen CAP parameters. Room certainly exists to further improve the treatment of electron emission with our code.

For the sake of illustration, we report here the irradiation of molecular nitrogen N_2 (aligned along the z-axis with bond distance 1.09 Å) with an XUV pulse and with a fast proton. We start our discussion with XUV irradiation. We apply a squared cosine-shaped pulse along the z-axis. The maximum electric field strength and energy of the XUV pulse are established at 0.005 Ha/bohr (3.5 x 10^{12} W/cm^2) and 30 eV, respectively. The total duration of the pulse is 30 fs. We have used the PBE XC functional [63]. The simulation was conducted for 50 fs with a time step of 1 as. A diffuse basis set built from the aug-cc-pVTZ but complemented with 28 diffuse functions was used [103].

The threshold distance $R°$, width W and maximum potential V^{max} of the spatial CAP are set to 15 Å, 5 Å, and 15 Ha, respectively. For the energy CAP, the energy scale γ_0 and damping strength ξ are set to 0.2 Ha and 0.05 Ha^{-1} respectively. The vacuum energy cut-off has been approximated as 0.0318 Ha so that the corrected energy of the lowest unoccupied MO equals the electron affinity calculated from two separate SCF calculations of the neutral and anionic forms of the molecule.

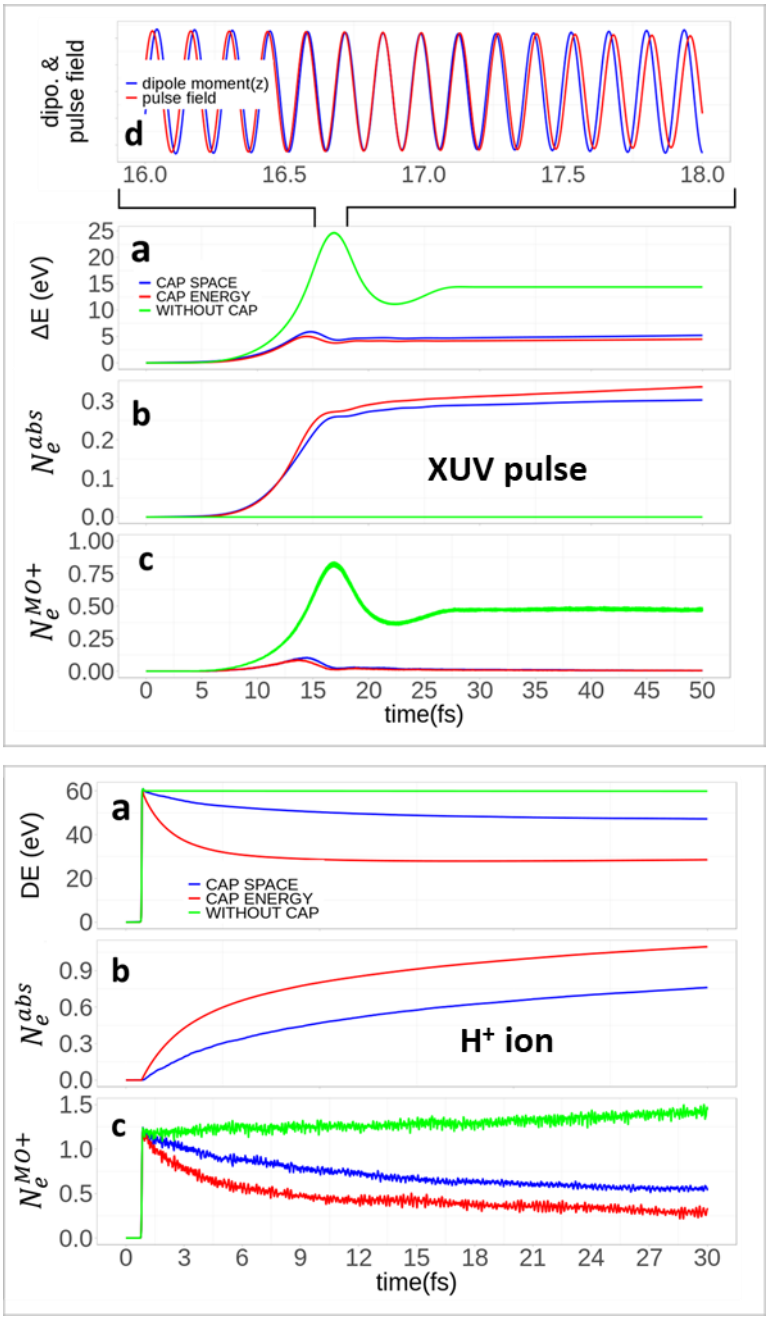

Figure 4: N_2 ionization by 30 eV XUV pulse (Top) and by an impact with a 0.07 MeV H^+ ion (Bottom). (a) variation of total energy (XUV-pulse), energy deposition (H^+ ion), (b) number of electrons absorbed by the CAP and (c) the numbers of electrons still in positive energy KS MOs, all as function of the simulation time (fs). (d) corresponds to the propagation of the dipole moment on the z axis and the pulse field between 16 and 18 fs. In order to easily compare the amplitude of the pulsed field is scaled.

Time-dependent profiles of the variation of total energy relative to the ground state (ΔE), of the number of absorbed electrons by the CAP (N_e^{abs}), and of the number of electrons in KS MOs of positive energy (N_e^{MO+}) are depicted in Figure 4. For simulations without CAP (green line), ΔE increases upon application of the pulse with a maximum at around 17 fs, then decreases and remains stable after application of the pulse. Panel *c* shows that the N_e^{MO+} curves follow the same evolution as ΔE. This feature arises when the delay of propagation of the dipole moment varies compared to the pulse field which produces destructive and constructive superpositions, as shown in Panel d. When adding a spatial or energy CAP, NBEs are quickly absorbed and the number of electrons is, as expected, no longer conserved (blue and red line) which also scales down ΔE, but both kinds of CAP give similar results. After a sharp increase at around 15 fs, when the external electric field is the most intense, a rather steady situation is obtained. In the end, the introduction of CAP was necessary to correctly describe the ionization and dynamics of the XUV pulse interaction. Either type of CAP can successfully remove the NBEs and decrease N_e^{MO+}.

We now consider the irradiation with a proton having 70 keV of kinetic energy. The same methodology and parameters are employed, except the CAP strength which is slightly modified: the threshold distance $R°$ of the spatial CAP was changed from 15.0 to 12.5 Å and, the energy scale γ_0 of energy CAP from 0.25 to 0.05 Ha. These modifications were needed to ensure the stabilization of the propagation. The proton was initially positioned 30 Å away from N_2 and struck the N-N bond after 816 as.

60 eV are deposited upon collision with the ion (Figure 4, bottom). In the absence of CAP, the energy is conserved after the collision, as expected for an isolated system. The number of electrons in positive energy KS MOs suddenly rises from 0 to 1.25 and smoothly increases up to 1.5 electrons. The sharp increase is clearly due to electronic excitations at the moment of the collision, while the slower phase is likely due to many internal electronic transitions taking place within the electron cloud (*e.g*. some auto-ionization processes). When a CAP is added, a fraction of electrons is absorbed, with a consequent reduction of total energy. CAP does not seem to affect much the amount of energy deposited by charged particles. This may be explained by the short interaction time compared to a photon pulse. On the other hand, the two flavors of CAP, either defined in spatial or in energy space, give different results. With the chosen parameters, the energy CAP absorbs electrons faster than the spatial CAP. The low energy electrons emitted upon collision need time to reach the $R°$ distance of the spatial CAP while they are more readily absorbed with the energy CAP after energy deposition. After 30 fs, the number of electrons and the total energy of the system haven't converged to the same values. One could probably tune the parameters of the energy CAP to match more closely the results obtained with the spatial CAP, for instance by decreasing the γ_0 term. It is actually hard to tell which

of the two CAP formulations is the most appropriate. This discussion illustrates the aforesaid comment on the use of CAP with deMon2k and the fact that more work is needed along this line.

3.2 Exchange-correlation functionals

The exact exchange-correlation functional appearing in the total energy expression in the Kohn-Sham formulation is unknown. In practice, different approximate XC functionals have been proposed and implemented in deMon2k software (see section 2.3).

Several issues are raised when using common functionals to simulate matter under strong perturbations. A prominent difficulty is the time dependence of the XC potential, $v_{xc}[\rho](\boldsymbol{r},t)$ that should incorporate memory effects from previous times. This time dependence is actually absent from most TD-DFT implementations, including ours. The adiabatic approximation becomes problematic when the system is brought far away from the ground state, as in the case of strong perturbation. Well-known limitations of adiabatic TD-DFT are the difficulty to describe multiple electron/hole transitions, and the inability to simulate charge migrations after photoionization [107]. Important efforts are made to go beyond the adiabatic approximation but the track is long and tedious [108–111].

Besides the time dependence of v_{xc}, another difficulty is the incorrect asymptotic decay of the exchange potential, which should decay as $-1/r$. A wrong asymptotic behavior was shown to severely underestimate high-lying excited states such as Rydberg states [42]. In addition, the improper treatment of the Derivative Discontinuity and of fractional occupations [112,113] are other sources of concern when dealing with charge migrations flowing in and out of atoms in large systems. In the past, we have used the correct-asymptotic-potential generalized-gradient-approximation functional developed by Carmona-Espíndola, Gázquez and co-workers[114]. Their recent “nearly correct CAP” exchange functional (NCAP)[115,116] that includes approximated the derivative discontinuity looks promising too.

Global hybrids functionals, as they adopt a fraction of exact exchange with the correct energy and potential asymptotic character, allow a more accurate description compared to their generalized-gradient-approximation counterpart. Nevertheless, the asymptotic decay of these XC functionals is modulated by a factor that ranges from 0 to 1 representing the amount of the exact exchange. As a consequence, the exchange potential decay will be underestimated depending on this factor and the one related to the DFT exchange. In range-separated hybrid functionals, the asymptotic decay of the potentials can be improved relative to their global hybrid counterparts, allowing a better description of a wide range of properties [117–119]. A physical justification of range-separated hybrid functionals was proposed by Savin in the 1990s [120,121]

Another drawback arising from the use of an approximate XC functional is the so-called self-interaction error [122]. The latter can be better illustrated considering a one-electron system in which the electron should experience only the external potential and for which we exactly know the KS potential and the total energy. In the ground state density, the system, which is assumed to be self-interaction free, should fulfill the following condition:

$$E_H[\rho_{i,\sigma}] - E_{XC}[\rho_{i,\sigma}] = 0 \qquad (15)$$

Over the years, several studies have shown how the self-interaction error can affect, for example, ionization processes [123], dissociation of molecules, and the prediction of the energy of charge-transfer states (the latter is further explored below). To address this issue, self-interaction correction (SIC) methods, based on the Perdew-Zunger correction [122], are frequently used. The latter involves the explicit subtraction of the self-interaction error for each orbital. An alternative is the average density SIC (ADSIC) [124], which assumes that the single electrons can be represented by equal single-particle densities, then replacing the single-electron density ρ_i with the averaged density ρ/N (with *N* the total number of electrons). ADSIC method is simple and shows good scaling properties with system size. It was shown to largely correct the ionization potential for a variety of atoms and molecules of different sizes and chemical compositions [125,126]. ADSIC was later tested in attosecond electron dynamics simulations with comparisons against time-dependent Schrodinger equation on top of correlated field-free stationary electronic states. RT-TD-DFT with ADSIC was found to perform qualitatively well in the case of strong but non-ionizing laser field irradiation [127]. On the other hand, a recent (RT-)TD-DFT study of a protein chromophore (bacterial chlorophyll) suggests that ADSIC still faces difficulties for charge transfer excited states [128].

Self-interaction error, together with the incorrect asymptotic behavior and the missing derivative discontinuity of XC functionals, can lead to an incorrect description of long-range charge transfer (CT) processes and charge recombination [129,130]. Computational tools have been developed to understand the reliability of TD-DFT approach in describing CT processes. A formula originally proposed by Mulliken [131] allows evaluating the lower excitation energy for one electron intermolecular CT (ω_{CT}) between a donor (D) and an acceptor (A):

$$\omega_{CT} = IP_D - EA_A - \frac{1}{R} \qquad (16)$$

IP_D is the ionization potential of the donor, EA_A is the electron affinity of the acceptor and 1/R represents the hole-electron coulombic interaction after CT. Inspired by this expression, the M_{AC} index [132,133], originally developed in linear response TD-DFT, uses a Koopman-type approach in which the

IP_D and EA_A are replaced by the weighted average of the starting (ϵ_i) and final (ϵ_a) DFT-Hartree-Fock orbital energies that are involved in the CT transition under analysis:

$$M_{AC} = \frac{\sum_{ia}[{c_{ia}}^2({\epsilon_a}^{DFT-HF} - {\epsilon_I}^{DFT-HF})]}{\sum_{ia} {c_{ia}}^2} - \frac{1}{D_{CT}} \quad (17)$$

The weights c_{ia} are the configuration interaction coefficients obtained as solutions of perturbative TD-DFT equations using Casida's formulation and the DFT- Hartree-Fock orbital energies are obtained with a single-cycle Hartree-Fock calculation on the converged SCF KS orbitals ${\epsilon_a}^{DFT-HF}$ and ${\epsilon_i}^{DFT-HF}$. This *ad hoc* correction aims at qualitatively correcting the underestimation of virtual orbitals due to self-interaction error as discussed in [133]. Finally, the geometrical distance between the donor and the acceptor units is replaced by the D_{CT} (distance of charge transfer) index, a descriptor able to quantify the degree of locality of a charge transfer process by giving an estimate of the hole-electron separation at the excited state only on the basis of the density redistribution upon the excitation [134]. The resulting *MAC* energy value represents in this way a lower bound to the transition energy related to the charge transfer state under analysis and the comparison of this value with the energy computed at TD-DFT level of theory allows the identification of unphysical states. If a given TD-DFT transition has an energy greater than the related M_{AC} energy, it will be associated with a real state, while a TD-DFT energy lower than the M_{AC} index will identify a ghost or a spurious state. Recently, some of us were involved in the modification of the M_{AC} index for simulation in the RT-TD-DFT domain [135]. The time-dependent M_{AC}^{RT} index at time t_j takes the following expression:

$$M_{AC}^{RT}(\mathrm{t_j}) = \frac{\sum_{virt}\left[n_{virt}(t_j){\epsilon_{virt}}^{DFT-HF}\right] - \sum_{occu}\left[n_{occu}(t_j){\epsilon_{occ}}^{DFT-HF}\right]}{\sum_{virt} n_{virt}(t_j) + \sum_{occu} n_{occu}(t_j)} - \frac{1}{\mathrm{D_{CT}}(\mathrm{t_j})} \quad (18)$$

where ϵ_{occu}^{DFT-HF} and ϵ_{virt}^{DFT-HF} are respectively the eigenvalues of the contributing occupied (starting) and virtual (final) molecular orbitals with single-cycle Hartree-Fock correction, while the weights $n_{virt}(t_j)$ and $n_{occu}(t_j)$ are the related occupation number at time t_j extracted on-the-fly during the electron dynamics. As well, the $\mathrm{D_{CT}}$ index is computed at every time t_j using the on-the-fly density snapshots. Finally, by comparing the set of M_{AC} energy values from $t_{initial}$ to t_{final} with the charge transfer state energy resulting from the dynamics, it is possible to assess which regions of the simulation derive from a correct or erroneous description of the process for a given exchange and correlation functional. We here report an example of the M_{AC}^{RT} application for a long-range charge transfer state simulation in RT-TD-DFT. In the latter study, the molecules under analysis are a family of typical push-pull systems containing two groups, one acting as an electron donor (-NH_2) and another

playing the role of electron acceptor (-NO_2), connected via a spacer of different lengths. We here consider as an example the molecule with three phenyl groups as a spacer in order to show the ghost states identification in a long-range CT process (Figure 5, left). After converging the ground state density via an SCF procedure, we applied a cos^2-shaped electric pulse fulfilling the π-pulse condition, namely $\boldsymbol{\mu_{0n}} \boldsymbol{F}_0 \int_{-\infty}^{+\infty} s(t)\, dt = \hbar\pi$, where $\boldsymbol{\mu_{0n}}$, $\boldsymbol{F}_0$ and s are the transition dipole moment, obtained by a separate Casida's equation TD-DFT calculation, the oscillatory electric field associated to the HOMO-LUMO transition and the envelop function, respectively [135]. The simulation has been done using an LDA functional in order to magnify the presence of ghost states.

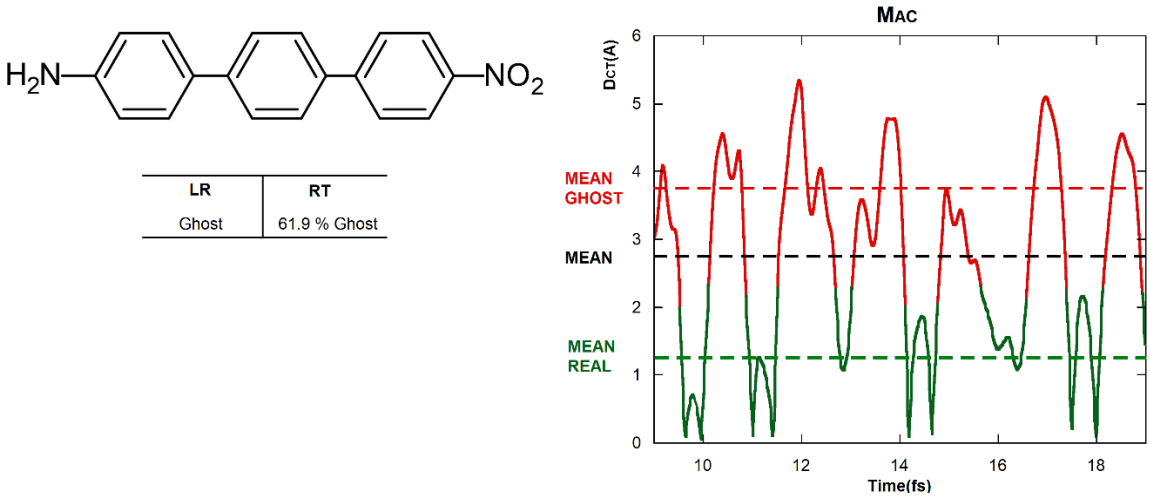

Figure 5: On the right: the CT distance (Å) in the regions of the simulation corresponding to real (green) and ghost states (red). Mean CT distance considering all data points of the simulation (dashed line in black), mean CT length values derived from the ghost (dashed line in red) and real states (dashed line in green). On the left: the molecule under analysis and a table showing the result of the MAC index applied on the transition energy of the CT state predicted in the TD-DFT approach and the percentage of ghost states predicted by the MAC index in the RT-TD-DFT simulation. Reproduced with permission from [135].

Figure 5 shows the evolution during the simulation of the distance of the charge transfer computed with DCT index for a time range of 10 fs. By computing the M_{AC}^{RT} index at the same timeframe and comparing it with the transition energy predicted during the RT simulation, we have been able to spot potential spurious states appearing during the dynamics. Indeed, the red color identifies time frames for which RT energies are expected to be incorrectly described with the LDA functional, while the green color is for time frames corresponding to correctly predicted RT energies. Overall, one can remark that the percentage of densities during the simulation corresponding to ghost states is higher than the real one, a result that agrees with the linear-response calculation that shows the presence of a low-lying CT ghost state. In summary, the M_{AC}^{RT} provides the researcher with a tool to identify those excited states that result to be erroneously shifted in energy, thus allowing to assess the reliability of the RT-

TD-DFT simulations. Note that the index is not able by itself to cure the presence of unphysical/ghost states which are caused by an inexact exchange-correlation potential.

4 Topological analyses of time-dependent electronic structures

Dedicated analysis tools are mandatory to extract insights from RT-TD-DFT electron dynamics simulations. deMon2k implements the calculation of atomic charges, and more generally intrinsic atomic multipole, up to quadrupole, moments following various partition schemes of the real space (Hirshfeld [136], Becke [137], Voronoi, …). To this end, numerical integrations of the electron density over the atoms are conducted at regular intervals along the simulation. As this task can become computationally intensive, the user has the possibility to tune the quality of the integration grid, and, more importantly, can substitute the Kohn-Sham density with the auxiliary density to extract atomic multipole moments, which is a very safe procedure in most cases [67]. Another kind of analysis is to project the time-dependent electronic structure onto the set of ground state MOs, providing information on the orbitals' population fluctuations over time. deMon2k can further generate specific files in "cube" format to visualize various molecular fields of interest such as the electronic density, the spin density, the electrostatic potential, the Kohn-Sham density currents, or the time-dependent electron localization function (TD-ELF) [138,139]. The cube file format can be read by many visualization software packages including VMD (*Visual Molecular Dynamics*) [140]. Finally, one can generate "wfn" files along the simulations as input to popular analysis packages such as Multiwfn [141] or Topchem2 [142].

We have proposed to extend the approach relying on the topological analysis of stationary electronic [143,144] structures to the time-dependent regime, focusing so far on the electron density and on TD-ELF [145,146]. Topological analyses of TD-ELF allow following changes in the Lewis structure under the effect of strong perturbation. TD-ELF incorporates a wealth of information on the time evolution of the chemical structures which allows the qualitative and quantitative characterization of the formation/breakage of bonds between atoms, the migration of charge between topological basins, and the eventual attachment of electron density to the projectile [146]. For the sake of illustration, Figure 6 shows the evolution of TD-ELF basins of a guanine nucleobase upon collision by a 1 MeV α-particle [146]. Just before collision (panel a), the electronic structure resembles that of the ground state with typical ELF topological basins, some being highlighted on the Figure. Immediately after collision (panel b), the disruption of the C=C central double bonds (showed in green characters) is clearly apparent, while the overall structure is recovered 400 as after (panel c) as a result of electronic

relaxation. The analysis also reveals the perturbation of other topological basins further away from the collision site, for example, the double C-O bond (V(C-O)) or nitrogen lone pairs (V(N)).

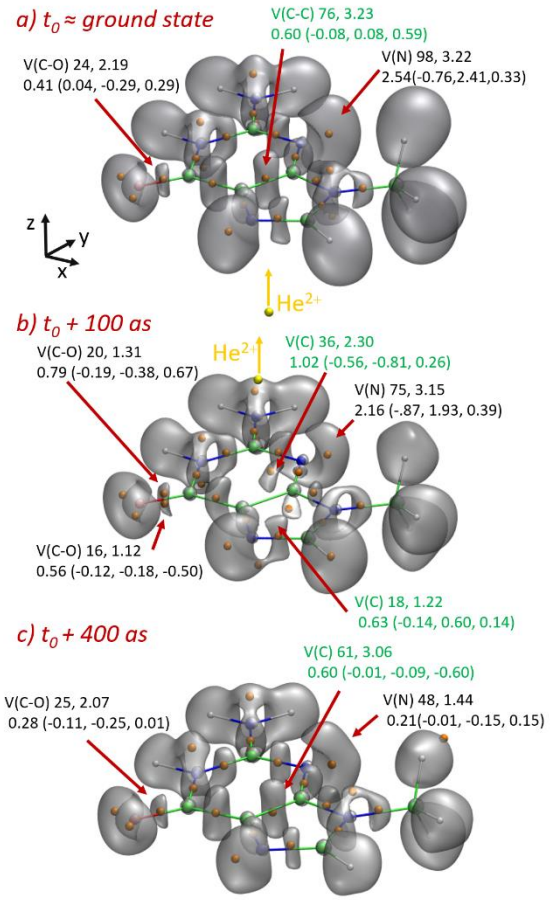

Figure 6: Topological analyses of TD-ELF after collision of guanine by a 1 MeV α particle traveling along the z direction. a-c: for each TD-ELF topological basin we indicate, in order, the volume (Å^3), the electronic population, and the intrinsic dipole moment (D, components in brackets). Collision is defined Color code: green: carbons, white: hydrogens, blue: nitrogen, red: oxygen, yellow: helium (α particle), and orange: off-nuclei ELF attractors. Adapted with permission from [146].

5 Mixed quantum-classical simulations

In this section, we describe two methodologies that are useful for modeling ultrafast phenomena when nuclear motion comes into play. Indeed, while RT-TD-DFT is a useful methodology to simulate the physical stage, albeit with limitations described above, nuclear motion inevitably becomes significant after a few femtoseconds and must be taken into account. Ehrenfest molecular dynamics (MD) is a natural extension of RT-TD-DFT whereby atom nuclei are moving in the mean-field potential created

by the superposition of electronic states provided by RT-TD-DFT. This methodology finds application to simulate the physicochemical stage. On the other hand, Born-Oppenheimer molecular dynamics (BOMD) assumes electrons stick to the ground state potential energy surface. BOMD is therefore more adapted to simulate the chemical stage. We emphasize that the *ab initio* MD research field is incredibly vast. We thus do not claim any exhaustivity here but only focus on some methods implemented in deMon2k so far for applications to radiation chemistry problems.

5.1 Born-Oppenheimer Molecular Dynamics

In theory, the exact description of a system is achieved if the time-dependent Schrödinger equation is solved for both nuclei and electrons. BOMD simplifies the problem using the Born-Oppenheimer approximation to deal with the electrons and nuclei independently. The electronic ground state energy is described by DFT while the nuclei dynamics are based on the classical equations of Newton. As for electron dynamics simulations, we introduce a time step Δt_N to propagate nuclear motion. With BOMD, one assumes that the relaxation of the electron cloud is instantaneous from one nuclear propagation step to another. In deMon2k, it is implemented [147,148] using the leapfrog method [3], which consists in the following steps: 1) Calculate mid-step velocities $\dot{\boldsymbol{R}}$ at $t + \frac{\Delta t_N}{2}$ (Eqn. 19), 2) calculate position vectors $\boldsymbol{R}$ at time $t + \Delta t_N$ (Eqn. 20), 3) calculate forces $\boldsymbol{F}$ at time $t + \Delta t_N$ (Eqn. 21), and finally 4) calculate velocities $\dot{\boldsymbol{R}}$ at time $t + \Delta t_N$ (Eqn. 22)

$$\dot{\boldsymbol{R}}\left(t + \frac{\Delta t_N}{2}\right) = \dot{\boldsymbol{R}}(t) + \left[\frac{\boldsymbol{F}(t)}{m}\right]\frac{\Delta t_N}{2} \tag{19}$$

$$\boldsymbol{R}(t + \Delta t_N) = \boldsymbol{R}(t) + \dot{\boldsymbol{R}}\left(t + \frac{\Delta t_N}{2}\right)\Delta t_N \tag{20}$$

$$\boldsymbol{F}(t + \Delta t_N) = -\boldsymbol{\nabla} E[\rho(r)] + Z_A \sum_{B \neq A} Z_B \frac{\boldsymbol{R}_A - R_B}{|R_A - R_B|^3} \tag{21}$$

$$\dot{\boldsymbol{R}}(t + \Delta t_N) = \dot{\boldsymbol{R}}\left(t + \frac{\Delta t_N}{2}\right) + \left[\frac{\boldsymbol{F}(t + \Delta t_N)}{m}\right]\frac{\Delta t_N}{2} \tag{22}$$

In these equations Z_X stands for the nuclear charge of atom X and *m* is the mass of the atom. The micro-canonical ensemble is often used due to its ease of implementation. However, it is easier to control temperature instead of energy during experiments and the systems are usually studied in the canonical ensemble. Several thermostats were thus implemented in deMon2k by Köster and collaborators to work in the canonical ensemble (Berendsen, Hoover or Nose-Hoover thermostats)[147].

We now illustrate the BOMD methodology with two applicative examples relevant to radiation chemistry. In the first example, we consider the difficult problem of Dissociative Electron Attachment. This is a well-known degradation reaction of molecules [6], however, the mechanism is complex and remains the topic of investigations using computational methods including molecular dynamics [149,150]. Kohanoff and co-workers proposed to approximate that the incoming electron, binds to the molecule and has time to relax to form a ground-state anion while the excess energy is transferred to a specific vibrational mode [151]. Let $\boldsymbol{R}_A$, $\boldsymbol{R}_B$ and $\dot{\boldsymbol{R}}_A^{(0)}, \dot{\boldsymbol{R}}_b^{(0)}$, be the initial position and velocity vectors of atoms A and B, η_A, η_B, the extra velocity vectors of atom A and B, and m_A, m_B, the masses of the atoms. The new velocities of atoms A and B after energy deposition are given by Eqn. 22.

$$\dot{\boldsymbol{R}}_A = \dot{\boldsymbol{R}}_A^{(0)} + \eta_A \hat{\boldsymbol{\mu}}\,; \quad \dot{\boldsymbol{R}}_B = \dot{\boldsymbol{R}}_B^{(0)} + \eta_B \hat{\boldsymbol{\mu}}(11) \tag{22}$$

$$\hat{\boldsymbol{\mu}} = \frac{\boldsymbol{R}_A - \boldsymbol{R}_B}{|\boldsymbol{R}_A - \boldsymbol{R}_B|} \tag{23}$$

The extra velocities are calculated from momentum conservation law given the gap energy ΔE between the resonant state and the lowest unoccupied molecular orbital:

$$\frac{1}{2} m_A \eta_A^2 + \frac{1}{2} m_B \eta_B^2 + m_A \eta_A \dot{\boldsymbol{R}}_A^{(0)} . \hat{\boldsymbol{\mu}} + m_B \eta_B \dot{\boldsymbol{R}}_B^{(0)} . \hat{\boldsymbol{\mu}} = \Delta E \tag{24}$$

$$m_A \eta_A + m_B \eta_B = 0 \tag{25}$$

The sum of equations 24 and 25 gives:

$$\frac{1}{2} m_A \left(1 + \frac{m_A}{m_B}\right) \eta_A^2 + m_A \left[\left(\dot{\boldsymbol{R}}_A^{(0)} - \dot{\boldsymbol{R}}_B^{(0)}\right) . \hat{\boldsymbol{\mu}}\right] \eta_A = \Delta E \tag{26}$$

with $\eta_B = -m_A \eta_A / m_B$. Under the approximation that $\Delta E \gg m_A \left[\left(\dot{\boldsymbol{R}}_A^{(0)} - \dot{\boldsymbol{R}}_B^{(0)}\right) . \hat{\boldsymbol{\mu}}\right] \eta_A$, one gets the following expression for the extra velocities:

$$\eta_A = \sqrt{\frac{2\Delta E}{m_A \left(1 + \frac{m_A}{m_B}\right)}}; \eta_B = \sqrt{\frac{2\Delta E}{m_B \left(1 + \frac{m_B}{m_A}\right)}} \tag{27}$$

Using this method, Kohanoff and co-workers investigated the consequences of low-energy electron attachment to the thymine nucleobase. They showed for example that the dissociation energy increases in the presence of a solvent as hydrogen bonds can form between solvent molecules and the system [151]. We refer the reader to [151,152] for more extensive studies on other molecules, including solvation effects. We have implemented this method in deMon2k and we illustrate it here

for the first time by considering DEA on tributylphosphate. This molecule is an organic extractant of Uranium (VI) and Plutonium (IV) used in the recycling process in the nuclear industry [153,154]. Assuming that a low-energy electron can attach to the phosphate group, an excess of 2.8 eV was injected into one of the three O-C bonds connected to it (Figure 7). A butyl radical is quickly ejected from the rest of the molecule in a few fs. The relative total charge of the ejected butyl chain increases by 0.32 while the one of the phosphate group decreases by the same quantity. The spin charge fully localizes on the leaving butyl moiety too, leaving a negatively charged dibutyl phosphate (data not shown). We observe charge oscillations between the phosphate group and the other butyl chains at longer times. After 60 fs, the radical part is 4 Å away from the anion and is not influenced by these atomic charge oscillations.

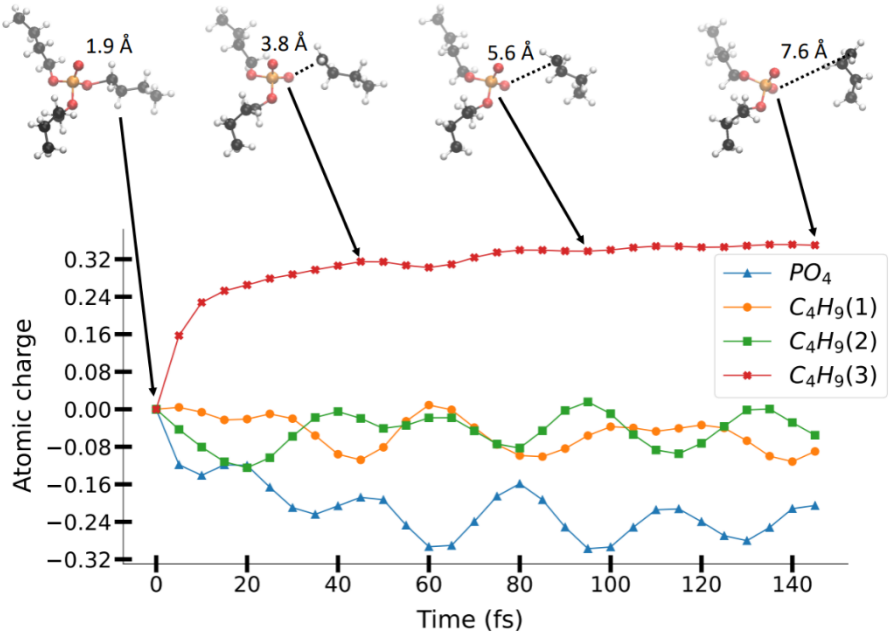

Figure 7: Dissociation of a butyl chain of tributylphosphate upon the addition of an electron bringing an excess of 2.8 eV in the C-O bond. BOMD simulations were carried out with the PBE0 XC functional and aug-cc-DZVP/GEN-A2 basis sets. The bond breaking is shown in the upper snapshots as a dark dotted line alongside the distance between the carbon and oxygen atoms.*

We come to a second example of the application of BOMD simulations we have reported recently [66]. In a campaign of picosecond time-resolved radiolysis of anionic uridine monophosphate (USP, standing for Uridine, Sugar, Phosphate), it was found that 5 ps after application of the ionizing pulse, no spectroscopic signature of the ionized nucleobase (U^+) moieties could be detected, pointing toward the existence of an ultrafast (< 5ps) charge transfer mechanism that would have reduced the ionized nucleobase ($U^+ \rightarrow U$). We investigated two distinct nuclear-driven charge transfer mechanisms. In the first one, we followed the Marcus theory of electron transfers and evaluated the free energy and free reorganization energy associated with the charge transfer from the phosphate group to the uracil

group (Figure 8, top). This was achieved by means of *constrained* DFT BOMD simulations [155]. Despite strong electronic coupling between the charge transfer electronic states (0.076 ± 0.017 eV), we found that a Marcus-theory-like electron transfer could not explain the reduction of U^+ on the sub-picosecond time scale. On the other hand, we discovered that a non-adiabatic relaxation could provide an explanation. Indeed, the topology of the potential energy surfaces creates the conditions that after ionization, the system relaxes on the U^+SP PES, crossing on the way the charge transfer USP^+ state (Figure 8, bottom). The hopping probability is significant and strongly depends on the electronic coupling between the states and on the electronic decoherence time scale. In summary, our numerical simulations provided a molecular explanation for intriguing experimental results [66,156].

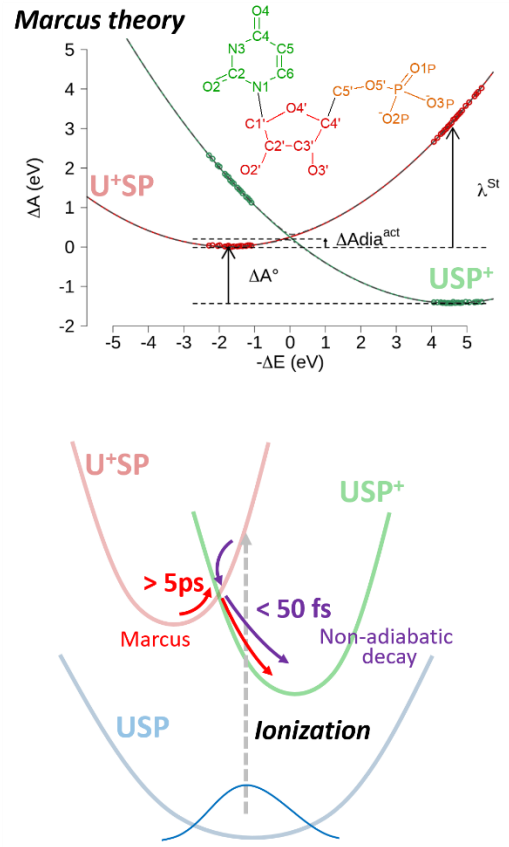

Figure 8: ab initio MD simulations using constrained DFT to explain the ultrafast reduction of ionized U^+SP. Top: Marcus theory modeling based on constrained DFT BOMD simulations between the U^+SP and USP^+ charge transfer states. Bottom: sketch of non-adiabatic decays following USP ionization, that competes with a Marcus electron transfer. Adapted with permission from [66].

5.2 Ehrenfest Molecular Dynamics

The physicochemical stage of irradiation may be described by TD-DFT-based Ehrenfest molecular dynamics (EMD), which is a mean-field scheme belonging to the so-called mixed quantum-classical methodologies [36,46,157,158]. This means that some degrees of freedom are treated quantum

mechanically (in this case, electrons) while others are treated in the classical mechanics limit. As in BOMD, atom nuclei are considered classical point particles to which Newton's equations-of-motion apply. However, while in BOMD the nuclear and electron degrees of freedom are treated in a self-consistent manner, by relaxing the electrons for every new nuclear configuration invoking the so-called adiabatic approximation, EMD attempts to couple electronic to nuclear degrees of freedom.

The time-dependent solution of the coupled equation-of-motions starts by defining the general TD Schrödinger equations for both nuclei (28) and electrons (29):

$$i\frac{\partial\Omega(\boldsymbol{R},t)}{\partial t} = -\frac{1}{2}\sum_{b}\frac{1}{m_b}\nabla^2_{\boldsymbol{R_b}}\Omega(\boldsymbol{R},t) + \left\{\int \Psi^*(\boldsymbol{r},t)\mathcal{H}_r(\boldsymbol{r},\boldsymbol{R})\Psi(\boldsymbol{r},t)\mathrm{d}\boldsymbol{R}\right\}\Omega(\boldsymbol{R},t) \tag{28}$$

$$i\frac{\partial\Psi(\boldsymbol{r},t)}{\partial t} = -\frac{1}{2}\sum_{a}\nabla^2_{\boldsymbol{r_a}}\Psi(\boldsymbol{r},t) + \left\{\int \Omega^*(\boldsymbol{R},t)V_{rR}(\boldsymbol{r},\boldsymbol{R})\Omega(\boldsymbol{R},t)\mathrm{d}\boldsymbol{R}\right\}\Psi(\boldsymbol{r},t) \tag{29}$$

The model introduces a feedback between the nuclear ($\Omega(\boldsymbol{R},t)$) and electron ($\Psi(\boldsymbol{r},t)$) states in the quantities in curly brackets. Since such quantities are integrated, the potential given by one type of particle acting on the other type of particle is averaged. This will represent a disadvantage if the simulation traverses a region of possible states with very different energies since one may end up with wave functions that do not represent a physically realistic situation for the system under study. Thus, it is highly recommended to apply EMD in situations where electron states are relaxed in a time scale much shorter than the time scale for nuclei or ultrafast processes triggered by strong intense laser fields. There are other limitations of EMD and alternatives have been proposed by the researchers to overcome them [159]. Interested readers are referred for example to the surface hopping [160] or exact factorization [28] mixed quantum-classical approaches.

Considering the difference in the typical time scales for electrons (attoseconds) and nuclei (femtoseconds), it is reasonable to implement the EMD in such a way that the nuclear equation-of-motion are not necessarily solved for every electron step (Δt_e). An interpolation scheme borrowed from Ref [158] is adopted: nuclear positions are propagated every Δt_N according to Newton's law using the forces acting on the nuclei (Eqn 19-22), while an intermediate time step (Δt_{Ne}) is introduced to interpolate nuclear positions between two nuclear steps. In this way, the energy gradients are calculated only every few Δt_N, reducing the overall computational cost. On the other hand, the values for Δt_e, Δt_{Ne} and Δt_N must be chosen with care to ensure energy conservation. As usual, the time steps should be small enough to resolve the physical phenomena to be simulated. A strong perturbation of the electronic degrees of freedom requires smaller time steps A first application of our EMD code was reported in Ref. [161] for the irradiation of a peptide by a 100 keV proton. In this

example, Δt_N was set to 20 as and Δt_{Ne} and Δt_e were both set to 0.33 as. We plan further applicative studies in the coming months.

6 Accounting for environment effects

So far, apart from the example of the USP molecule, we have discussed molecular systems in the gas phase, but most problems of interest in radiation chemistry take place in the condensed phase. We describe below the methodologies available in deMon2k to account for environment effects. We describe here the hybrid QM/MM methodology using either non-polarizable or polarizable force fields.

6.1 Hybrid QM/MM

The QM/MM methodology, *i.e* the combination of quantum chemical (QM) and molecular mechanics (MM) simulation methods, was initially formulated in 1976 by Warshel and Levitt [162], with the aim to extract the best of both worlds: the accuracy of QM methods (semi-empirical [163], Kohn-Sham Density Functional Theory [40] or wavefunction methods) and the applicability of force-field-based MM[164] to a large number of atoms. Its continued relevance to chemical, and especially biochemical, questions means that it is still the subject of developments and implementations today (see non-exhaustively [161,165–168]).

Indeed, for inhomogeneous atomic systems, such as those that can be separated into a « QM region » which requires a description of its electronic structure and an « MM region » for which atomic positions and electrostatic interactions constitute a sufficient description, there is a need for a method bridging the gap between the too expensive DFT/wavefunction methods and the too inaccurate MM/MD. The crux of the problem here is the computational cost of representing the full chemical system at a quantum chemical level of accuracy, *i.e* with its electron density in the case of DFT or its wavefunction in post-Hartree-Fock methods. A typical strategy to treat a system with the QM/MM methodology would be to limit the « QM region » of interest to the order of 10^0 to 10^3 atoms, while the « MM region » would contain the rest of the protein or macromolecule, and as much solvent as needed to properly reproduce the system of interest.

The in-deMon2k QM/MM implementation [168] follows an additive scheme, or electrostatic embedding [169]. It was historically implemented by A. G. Goursot†, and later developed in our group for modeling complex biological systems [161]. In such a setup, and choosing DFT as our method of choice to evaluate the energy of the QM region, the total energy of the system can be computed in several ways. In this scheme, the total energy $E^{QM/MM}[\rho]$ expression in equation 30 is composed of

three terms: the energy of the QM region $E^{QM}[\rho]$, the energy of the MM region E^{MM}, and the interaction energy between the QM and MM regions $E^{QM*MM}[\rho]$.

$$E^{QM/MM}[\rho] = E^{QM}[\rho] + E^{MM} + E^{QM*MM}[\rho] \quad (30)$$

In deMon2k, the energy of the QM region is determined at the ADFT (Eqn. 30) or RT-TD-ADFT levels that were explained in section 2.2. As the atoms in the MM region are described as classical particles, the total energy is a function of the force field applied to them. Eqn. 31-33 bring the main types of interaction together: the bonded and non-bonded interactions. On one hand, E^{bonded} includes bond energies E^{bond}, bond-angles energies E^{angle}, torsion-angle energies $E^{torsion}$, and improper dihedral-angle energies $E^{improper}$. On the other hand, the non-bonded energies $E^{non-bonded}$ are described by the sum of Coulomb's law energy E^{elec} and a Lennard-Jones potential E^{LJ} for the van der Waals interactions.

$$E^{MM} = E^{bonded} + E^{non-bonded} \quad (31)$$

$$E^{bonded} = E^{bond} + E^{angle} + E^{torsion} + E^{improper} \quad (32)$$

$$E^{non-bonded} = E^{elec} + E^{LJ} \quad (33)$$

deMon2k implements the OPLS [170] or Amber [171] force fields to define the explicit form of the bonded terms. The interaction energy makes the connection between the QM and the MM regions (Eqn 35). It is formed by the interaction energy between the electron density ρ of the QM region and the atomic charges q_K of the MM region, then the Coulomb interaction energy E^{Zq} between MM atomic charges q_K and nuclei Z_A of the QM region, and the sum of the Lennard-Jones interactions between MM and QM atoms.

$$E^{QM*MM}[\rho] = E^{pq} + E^{Zq} + E^{LJ} \quad (34)$$

$$E^{QM*MM}[\rho] = -\sum_{K}^{MM} \int \frac{q_K . \rho(r)}{|r - R_K|} dr + \sum_{A}^{QM} \sum_{K}^{MM} \left[\frac{q_K . Z_A}{|R_{AK}|} + \varepsilon_{AK} \left[\left(\frac{r_{AK}^{min}}{R_{AK}} \right)^{12} - 2 \left(\frac{r_{AK}^{min}}{|R_{AK}|} \right)^{6} \right] \right] \quad (35)$$

Since E^{QM*MM} depends explicitly on ρ, the external potential includes a contribution from the external MM charges. It is often the case that the boundary between QM and MM region cuts through a covalent bond; in such cases, link atoms or tuned pseudo-potentials are available with deMon2k [161].

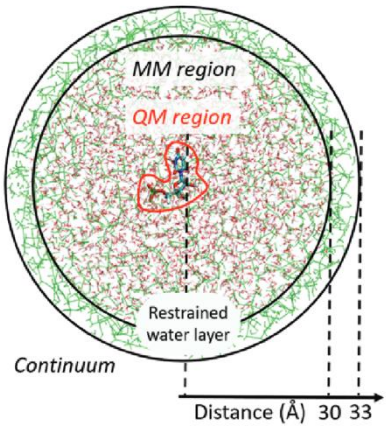

Figure 9: Typical QM/MM setup in deMon2k adapted to run MD simulations. Reproduced with permission from [66].

For large solvated systems such as that shown in Figure 9, a convenient way to model long-range effects in a QM/MM simulation is to enclose the MM part, which contains mainly solvent molecules, into a polarizable continuum solvent medium, such as the Onsager continuum [172]. A major development carried out in our group has been the QIB program (QM/MM Input Builder). QIB interfaces popular MM packages for bio-simulations (AMBER [171], CHARMM [173], TINKER-HP [174], GROMACS [175]…) to deMon2k [176]. It is now straightforward to prepare input files for RT-TD-ADFT, BOMD, or Ehrenfest MD with QM/MM on complex biological structures (DNA/protein complexes, proteins embedded in a membrane, …).

Figure 10 illustrates some results obtained about the physical stage of irradiation of solvated oligonucleotides with fast ions [66]. We identified a mechanism that we named "ebb-and-flow ionization" by which the incoming projectile polarizes the electron cloud prior to the collision, inducing an accumulation of electron density on the collided molecules. This effect is known experimentally as the Barkas effect [177]. Among other results, we identified that secondary electrons tend to attach to nucleobases and on the ribose, but also in the first solvation shell. Variations of the irradiation conditions, mass or kinetic energy of the projectiles, significantly affect the ionization probabilities (Figure 10, bottom). More insights can be found in the original publication.

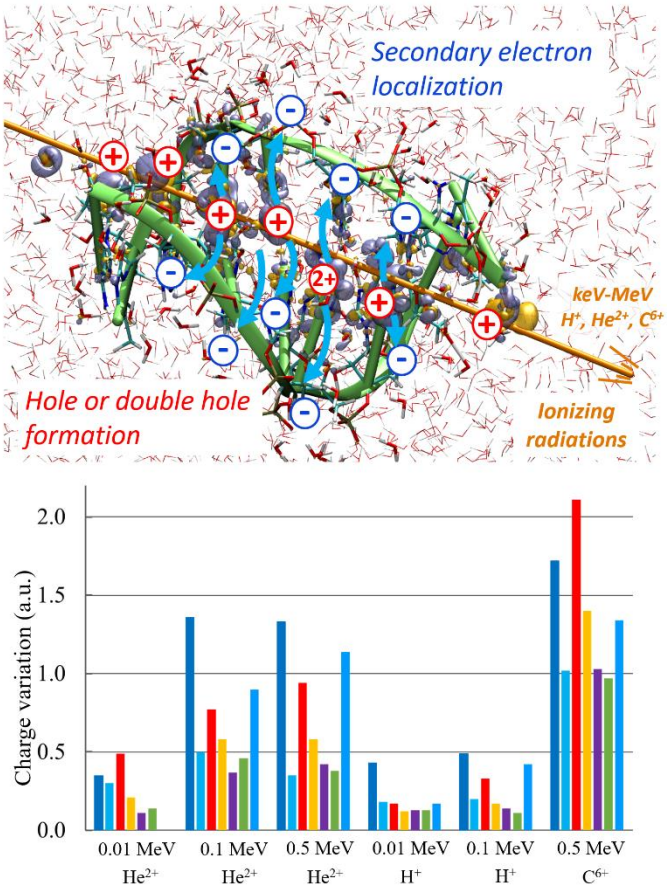

Figure 10: RT-TD-ADFT/MM simulations have given access to key insights into solvated DNA irradiation by swift ions. Top: simulated system, the entire DNA, and the first solvation shell are described by DFT. Bottom: the amount of electron depletion on 7 molecular moieties encountered by the projectiles on their path (3 water molecules in blue, thymine in red, cytosine in orange, and two guanine-cytosine pairs in green and violet). Different projectile properties are compared. Reproduced with permission from [80].

6.2 Going beyond the static embedding picture

A further improvement in the description of the environment in a QM/MM framework can be achieved by the use of polarizable force fields [178]. A possible way is to assign to each polarizable site within the MM region, typically atoms, an induced dipole that depends on the polarization state of the electron cloud in the QM region. In the context of coupling RT-TD-DFT simulations to polarizable MM force fields, we showed that a point-charge-dipole model of induction whereby each induced dipole is calculated as the product of a static and isotropic atomic polarizability with the electric field on the MM atom is sufficient to deal with embedded systems subjected to strong field irradiations [179,180]. It is not needed to involve frequency dependence in atomic polarizabilities, nor to consider higher order terms depending on the first or second hyperpolarizabilities [179]. In this QM/MMpol scheme, the QM region perturbs the polarizable MM environment in real-time, and, as a back reaction, the polarizable MM environment can affect the electron dynamics by the inclusion of the potential created by induced dipoles into the Kohn-Sham potential. Here again the availability of electron fitted densities

helps to drastically reduce the cost of the QM/MM interaction calculations. We have described our methodology at length in various publications. We refer the interested reader to previous publications for details [61,180]. We instead focus here on two applicative studies.

In [180], we highlighted various regimes governing the dynamics of electronic polarization within a solute's solvation shells as a function of the distance to the solute (Figure 11). The electron density residing on the solute was perturbed by a narrow electric kick (F_{max}), the strength of which was varied and set here to 0.01 a.u., and the subsequent average induced dipole ($\Delta\mu$) on water molecules was monitored in real-time. The response of the environment to the perturbation was shown to be dependent on the distance to the molecule: the further away, the weaker the response. Induced dipole moment oscillations are damped over time (Middle panel of Figure 11) as a result of energy dissipation with the MMpol region. The induced-dipole autocorrelation function revealed insights into the response mechanisms that depend on the electric fields generated by the electron density on the QM region and by the fluctuating MM-induced dipoles on the polarizable water molecules (Bottom). We refer the interested reader to Ref. [180] for a detailed analysis. In a following article [62], we introduced relativistic delays in the propagation of electric fields mediating the QM*MMpol interactions. We found these effects small for the kind of perturbation investigated (*i.e.* narrow electric kicks on the QM region).

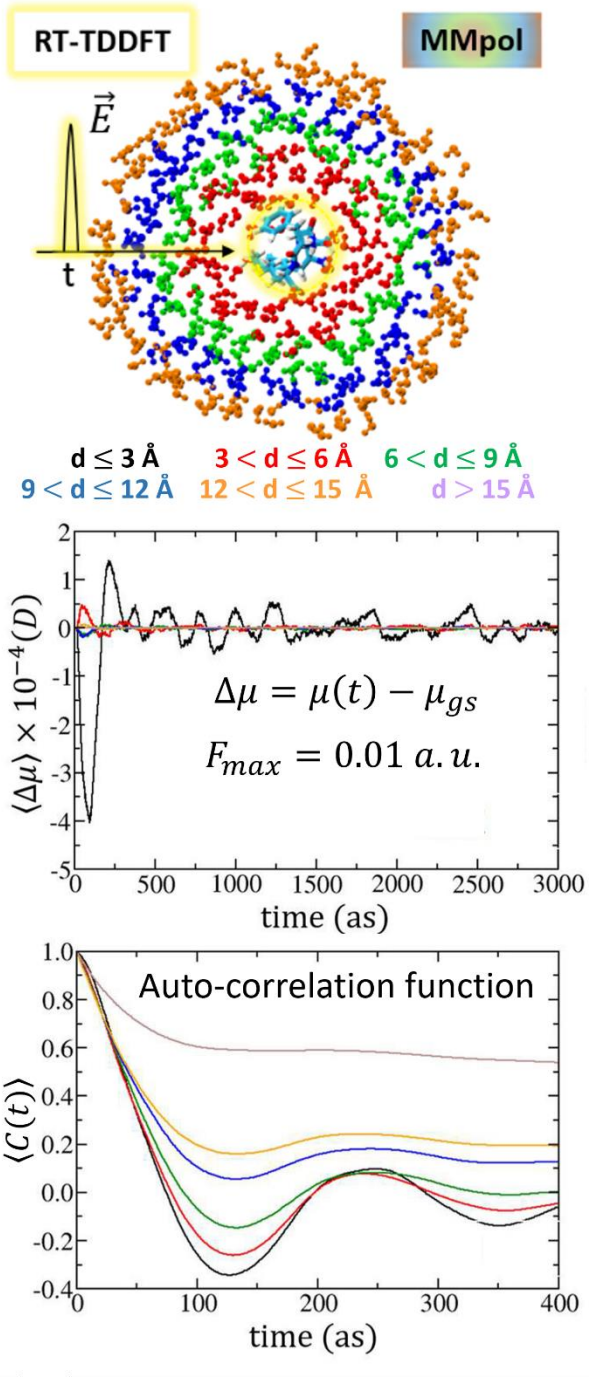

Figure 11: After perturbation of the solute, here a peptide described at the RT-TD-ADFT level, by a narrow electric pulse, the solvation shells, described by a polarizable force field respond in a distance-dependent manner via complex mechanisms. Top: color code defining the solvation layers by distance. Middle: mean variation of water dipole moments by solvation layer with respect to the ground state. Bottom: auto-correlation function of curves plotted in the middle panel. Adapted with permission from [180].

We have investigated polarizable embedding effects in the context of large biological systems irradiation with fast ions. First, we considered as targets the phosphate backbone of the DNA model shown in Figure 10 [181], and a DNA-protein complex [61]. We found for both systems that induction within the MM region does not affect energy deposition, nor the ultrafast responses of the electron cloud (charge migrations) in the following femtoseconds. This result can be understood by the fact that

energy deposition is driven by Coulomb interactions between the projectile and the electron cloud and is a very local property.

The variations of Kohn-Sham energy, relative to the ground state (energy deposition), over time are depicted in (Figure 12) in the polarizable and non-polarizable simulations. When the α-particle interacts with the electron cloud of the system, after a few attoseconds, it deposits its energy which leads to sharp excitation and ionization. The use of a polarizable force field has only a small effect on energy deposition, with a tiny rise of about 1 eV compared to our previous work with a much larger QM region. The difference is negligible compared to the high deposited energy of 238 eV. Since the process of energy transition from the charged particle is very fast, induction on MMpol region is not significant.

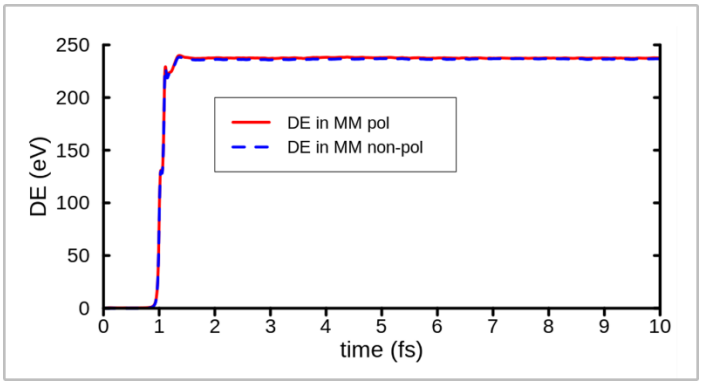

Figure 12: Energy deposition over 10 fs as a result of the collision of 0.25 MeV He^{+2} with DNA protein complex in a polarizable force field (red solid line) and non-polarizable force field (dash blue line).

The environment merely has a polarization effect on the ground state density. In particular, for the DNA/protein complex, no differences could be seen in post-collision charge fluctuations (Figure 13). Note that in our previous simulations, the environment close to the struck molecular moieties was included in the QM region, pushing away the polarizable MM region and, hence, decreasing the likelihood that induction could have a role on the very site of irradiation. For the present article, we thus repeat our simulations on the DNA/protein complex, reducing the size of the QM region from 342 to 102 atoms. The layer now encompasses three amino acids (ASP-ARG-THR), one nucleotide T, and four water molecules. The rest of the system is described with the polarizable Amberff02 force field [182]. An α-particle with kinetic energy of 0.25 MeV, is initially placed 40 Å away from the center of mass of the QM region. During the simulation, the α-particle travels through the QM region and strikes the backbone between the aspartate and arginine residues.

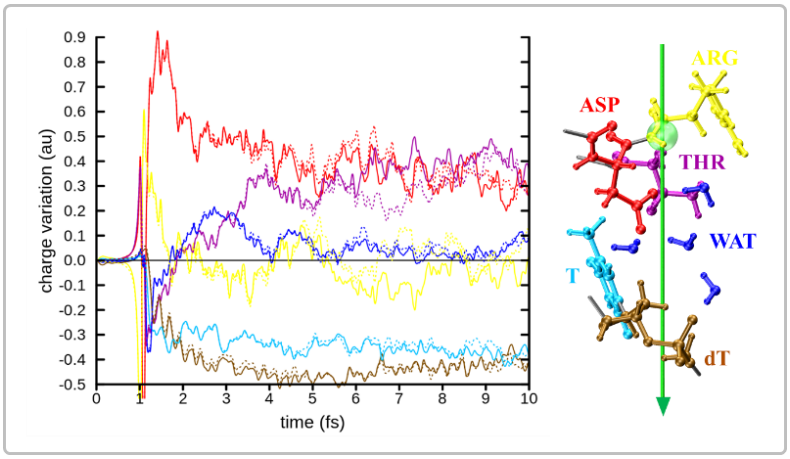

Figure 13: Left, charge variation of nucleoprotein complex (left) with a polarizable (solid lines) and non-polarizable (dashed lines) force field environment over 10 fs. Right: represents the QM region irradiated by the α-particle (green line); the green bead indicates the collision site of the α-particle with the protein backbone. The color codes refer to the fragments: ASP, aspartate (red); ARG, arginine (yellow); THR, threonine (purple); T, thymine base (cyan); dT, thymine-sugar moiety (brown); and WAT, water molecules (blue).

We show in Figure 13 the charge variation on the fragments along the simulation taking the electronic ground state as a reference. Charge fluctuations start during the approaching of the projectile (that is, before the impact). An ebb-and-flow mechanism of ionization is again at play, as seen from the decrease/increase charge variation at the moment of collision (0.8 – 1.3 fs). As already reported, this initial phase is insensitive on the incorporation of electronic induction on the MM region. On longer time, partial holes formed on ASP and ARG migrate to the surrounding media and delocalize over other fragments. The introduction of MM induction affects charge flows on ARG and THR a few femtoseconds after irradiation (yellow and violet lines). This can be understood as the side chains of ARG and THR are more polar and directly exposed to the MM environment.

7 Conclusions and perspectives

In this article, we have reviewed recent developments made in deMon2k to simulate the early stages of biological matter subjected to ionizing radiations. Of course, the road is long before having at hand all the tools needed to tackle adequately the great challenges posed by ionizing radiation interacting with inhomogeneous matter. The ADFT-based methodologies have already permitted to obtain new and encouraging results. deMon2k now offers a range of well-integrated simulation techniques including electron dynamics and molecular dynamics simulations in the ground and excited states (BOMD and Ehrenfest MD), including nuclear quantum effects with multicomponent DFT, as well as a coupling to polarizable force fields for hybrid QM/MM simulations. It runs on HPC architectures using either CPU or GPU machines. The code is available for interested users on request to the authors, keeping in mind that the modules are progressively integrated into the public version of deMon2k[49].

Pure RT-TD-ADFT simulations of large biomolecules have shed light on the physical stage of ionizing radiation, revealing the so-called ebb-and-flow mechanism of ionization by fast ions and other valuable insights into the location of secondary electrons. We also deployed these simulation tools in various applicative studies to help the interpretation of pulse radiolysis studies. Applications to XUV ionization of large biological structures have been carried out and will be reported soon. New developments are underway in our laboratories either to further improve the computational performance, improve the reliability of TD-ADFT simulations, or to devise new approaches to reach more realistic simulations.

Acknowledgements

We are grateful to GENCI (France) and Digital Research Alliance of Canada for continuous support by allocating generous access to HPC facilities. We are grateful to our collaborators for many stimulating discussions, notably Prof. D.R. Salahub (University of Calgary, Canada), Dr. A. M. Köster (CINVESTAV, Mexico), Prof. M. Mostafavi (Université Paris-Saclay, France), Dr. I Ciofini (Chimie Paris Tech, France), Dr. J. Pilmé (Sorbone Université, France), Dr. F. Lepine (Université Claude Bernard, France) and Dr. D Guillaumont (CEA Marcoule, France). We are grateful to the reviewers for their insightful comments. This work was supported by the French *Agence Nationale de la Recherche* (Project RUBI, number: ANR-19-CE29-0011-01).

Data Availability Statement

No Data associated in the manuscript.

References

[1] Mozumder A 2003 Interaction of Fast Charged Particles with Matter *Charged Particle and Photon Interactions with Matter* (CRC Press)

[2] Lacombe S, Porcel E and Scifoni E 2017 Particle therapy and nanomedicine: state of art and research perspectives *Cancer Nanotechnology* **8** 9

[3] Bourhis J, Sozzi W J, Jorge P G, Gaide O, Bailat C, Duclos F, Patin D, Ozsahin M, Bochud F, Germond J-F, Moeckli R and Vozenin M-C 2019 Treatment of a first patient with FLASH-radiotherapy *Radiotherapy and Oncology* **139** 18–22

[4] Savolainen J, Uhlig F, Ahmed S, Hamm P and Jungwirth P 2014 Direct observation of the collapse of the delocalized excess electron in water *Nature Chemistry* **6** 697

[5] Alizadeh E and Sanche L 2012 Precursors of Solvated Electrons in Radiobiological Physics and Chemistry *Chem. Rev.* **112** 5578–602

[6] Elahe Alizadeh, Thomas M. Orlando and Léon Sanche 2015 Biomolecular Damage Induced by Ionizing Radiation: The Direct and Indirect Effects of Low-Energy Electrons on DNA *Annu. Rev. Phys. Chem.* **66** 379–98

[7] Anon 2006 *Free-Radical-Induced DNA damage and its repair* (Berlin Heidelberg: Spinger-Verlag)

[8] Becker D, Adhikary A and Sevilla M 2010 Physicochemical Mechanisms of Radiation-Induced DNA Damage *Charged Particle and Photon Interactions with Matter* (CRC Press) pp 503–41

[9] Lorat Y, Brunner C U, Schanz S, Jakob B, Taucher-Scholz G and Rübe C E 2015 Nanoscale analysis of clustered DNA damage after high-LET irradiation by quantitative electron microscopy – The heavy burden to repair *DNA Repair* **28** 93–106

[10] Stingele J and Jentsch S 2015 DNA–protein crosslink repair *Nature Reviews Molecular Cell Biology* **16** 455

[11] Baulch J E 2018 Radiation-induced genomic instability, epigenetic mechanisms and the mitochondria: a dysfunctional ménage a trois? *Int. J. Radiat Biol.* 1–9

[12] Szumiel I 2015 Ionizing radiation-induced oxidative stress, epigenetic changes and genomic instability: The pivotal role of mitochondria *Int. J. Radiat Biol.* **91** 1–12

[13] Nisoli M, Decleva P, Calegari F, Palacios A and Martín F 2017 Attosecond Electron Dynamics in Molecules *Chem. Rev.* **117** 10760–825

[14] Loh Z-H, Doumy G, Arnold C, Kjellsson L, Southworth S H, Al Haddad A, Kumagai Y, Tu M-F, Ho P J, March A M, Schaller R D, Bin Mohd Yusof M S, Debnath T, Simon M, Welsch R, Inhester L, Khalili K, Nanda K, Krylov A I, Moeller S, Coslovich G, Koralek J, Minitti M P, Schlotter W F, Rubensson J-E, Santra R and Young L 2020 Observation of the fastest chemical processes in the radiolysis of water *Science* **367** 179

[15] Calegari F, Ayuso D, Trabattoni A, Belshaw L, De Camillis S, Anumula S, Frassetto F, Poletto L, Palacios A, Decleva P, Greenwood J B, Martín F and Nisoli M 2014 Ultrafast Electron Dynamics in Phenylalanine Initiated by Attosecond Pulses *Science* **346** 336–9

[16] Periyasamy G, Levine R D and Remacle F 2009 Electronic wave packet motion in water dimer cation: A many electron description *Chem. Phys.* **366** 129–38

[17] Marante C, Klinker M, Corral I, González-Vázquez J, Argenti L and Martín F 2017 Hybrid-Basis Close-Coupling Interface to Quantum Chemistry Packages for the Treatment of Ionization Problems *J. Chem. Theor. Comput.* **13** 499–514

[18] Jagau T-C, Bravaya K B and Krylov A I 2017 Extending Quantum Chemistry of Bound States to Electronic Resonances *Annu. Rev. Phys. Chem.* **68** 525–53

[19] Omar K A, Hasnaoui K and de la Lande A 2021 First-Principles Simulations of Biological Molecules Subjected to Ionizing Radiation *Annu. Rev. Phys. Chem.* **72** 445–65

[20] Miteva T, Kazandjian S and Sisourat N 2017 On the computations of decay widths of Fano resonances *Chemical Physics* **482** 208–15

[21] Coccia E and Luppi E 2021 Time-dependent ab initio approaches for high-harmonic generation spectroscopy *Journal of Physics: Condensed Matter* **34** 073001

[22] Cireasa R, Boguslavskiy A E, Pons B, Wong M C H, Descamps D, Petit S, Ruf H, Thiré N, Ferré A, Suarez J, Higuet J, Schmidt B E, Alharbi A F, Légaré F, Blanchet V, Fabre B, Patchkovskii S, Smirnova O, Mairesse Y and Bhardwaj V R 2015 Probing molecular chirality on a sub-femtosecond timescale *Nature Physics* **11** 654–8

[23] Beaulieu S, Comby A, Clergerie A, Caillat J, Descamps D, Dudovich N, Fabre B, Géneaux R, Légaré F, Petit S, Pons B, Porat G, Ruchon T, Taïeb R, Blanchet V and Mairesse Y 2017 Attosecond-resolved photoionization of chiral molecules *Science* **358** 1288–94

[24] Gruson V., Barreau L., Jiménez-Galan Á., Risoud F., Caillat J., Maquet A., Carré B., Lepetit F., Hergott J.-F., Ruchon T., Argenti L., Taïeb R., Martín F., and Salières P. 2016 Attosecond dynamics through a Fano resonance: Monitoring the birth of a photoelectron *Science* **354** 734–8

[25] Gao C-Z, Dinh P M, Reinhard P-G and Suraud E 2015 On time-resolved electron emission at the attosecond time scale *J. Phys. Conf. Ser.* **635** 012007

[26] Vacher M, Bearpark M J and Robb M A 2016 Direct methods for non-adiabatic dynamics: connecting the single-set variational multi-configuration Gaussian (vMCG) and Ehrenfest perspectives *Theoretical Chemistry Accounts* **135** 187

[27] Merritt I C D, Jacquemin D and Vacher M 2021 Attochemistry: Is Controlling Electrons the Future of Photochemistry? *J. Phys. Chem. Lett.* **12** 8404–15

[28] Pieroni C and Agostini F 2021 Nonadiabatic Dynamics with Coupled Trajectories *J. Chem. Theory Comput.* **17** 5969–91

[29] Agostini F and Gross E K U 2021 Ultrafast dynamics with the exact factorization *Eur. Phys. J. B* **94** 179–93

[30] Worth G A and Lasorne B 2020 Gaussian Wave Packets and the DD-vMCG Approach *Quantum Chemistry and Dynamics of Excited States* pp 413–33

[31] Joubert-Doriol L 2022 Variational Approach for Linearly Dependent Moving Bases in Quantum Dynamics: Application to Gaussian Functions *J. Chem. Theory Comput.* **18** 5799–809

[32] Castro P J, Perveaux A, Lauvergnat D, Reguero M and Lasorne B 2018 Ultrafast internal conversion in 4-aminobenzonitrile occurs sequentially along the seam *Chemical Physics* **509** 30–6

[33] Mendive-Tapia D, Firmino T, Meyer H-D and Gatti F 2017 Towards a systematic convergence of Multi-Layer (ML) Multi-Configuration Time-Dependent Hartree nuclear wavefunctions: The ML-spawning algorithm *Chemical Physics* **482** 113–23

[34] Mangaud E, Lasorne B, Atabek O and Desouter-Lecomte M 2019 Statistical distributions of the tuning and coupling collective modes at a conical intersection using the hierarchical equations of motion *J. Chem. Phys.* **151** 244102

[35] Chin A W, Mangaud E, Chevet V, Atabek O and Desouter-Lecomte M 2019 Visualising the role of non-perturbative environment dynamics in the dissipative generation of coherent electronic motion *Chemical Physics* **525** 110392

[36] Hervé du Penhoat M-A, Moraga N R, Gaigeot M-P, Vuilleumier R, Tavernelli I and Politis M-F 2018 Proton Collision on Deoxyribose Originating from Doubly Ionized Water Molecule Dissociation *J. Phys. Chem. A* **122** 5311–20

[37] Gaigeot M P, Lopez-Tarifa P, Martin F, Alcami M, Vuilleumier R, Tavernelli I, Hervé du Penhoat M A and Politis M F 2010 Theoretical investigation of the ultrafast dissociation of ionised biomolecules immersed in water: Direct and indirect effects *Mut. Res.Rev. Mut. Res.* **704** 45–53

[38] Bignon E, Gillet N, Jiang T, Morell C and Dumont E 2021 A Dynamic View of the Interaction of Histone Tails with Clustered Abasic Sites in a Nucleosome Core Particle *J. Phys. Chem. Lett.* **12** 6014–9

[39] Hohenberg P and Kohn W 1964 Inhomogeneous electron gas *Physical Review* **136** B864–71

[40] Kohn W and Sham L J 1965 Self-consistent equations including exchange and correlation effects *Phys. Rev.* **140** A1133–8

[41] Runge E and Gross E K U 1984 Density-Functional Theory for Time-Dependent Systems *Phys. Rev. Lett.* **52** 997–1000

[42] Mark E. Casida, Christine Jamorski, Kim C. Casida and Dennis R. Salahub 1998 Molecular excitation energies to high-lying bound states from time-dependent density-functional response theory: Characterization and correction of the time-dependent local density approximation ionization threshold *J. Chem. Phys.* **108** 4439–49

[43] Yabana K and Bertsch G F 1996 Time-dependent local-density approximation in real time *Phys. Rev. B* **54** 4484–7

[44] Domps A, Reinhard P G and Suraud E 1998 Time-Dependent Thomas-Fermi Approach for Electron Dynamics in Metal Clusters *Phys. Rev. Lett.* **80** 5520–3

[45] Theilhaber J 1992 Ab initio simulations of sodium using time-dependent density-functional theory *Phys. Rev. B* **46** 12990–3003

[46] Tavernelli I, Gaigeot M-P, Vuilleumier R, Stia C, Hervé du Penhoat M-A and Politis M-F 2008 Time-Dependent Density Functional Theory Molecular Dynamics Simulations of Liquid Water Radiolysis *ChemPhysChem* **9** 2099–103

[47] Li X, Govind N, Isborn C, DePrince A E and Lopata K 2020 Real-Time Time-Dependent Electronic Structure Theory *Chem. Rev.* **120** 9951–93

[48] Gómez Pueyo A, Marques M A L, Rubio A and Castro A 2018 Propagators for the time-dependent Kohn-Sham equations: multistep, Runge-Kutta, exponential Runge-Kutta, and commutator free Magnus methods *J. Chem. Theor. Comput.* 3040–52

[49] Köster A M, Geudtner G, Alvarez-Ibarra A, Calaminici P, Casida M E, Carmona-Espindola J, Dominguez V, Flores-Moreno R, Gamboa G U, Goursot A, Heine T, Ipatov A, de la Lande A, Janetzko F, del Campo J-M, Mejia-Rodriguez D, Reveles J, Vasquez-Perez J, Vela A, Zuniga-Gutierrez B and Salahub D R 2018 deMon2k Version 5

[50] Li X, Smith S M, Markevitch A N, Romanov D A, Levis R J and Schlegel H B 2005 A time-dependent Hartree-Fock approach for studying the electronic optical response of molecules in intense fields *Phys. Chem. Chem. Phys.* **7** 233–9

[51] Lopata K and Govind N 2011 Modeling Fast Electron Dynamics with Real-Time Time-Dependent Density Functional Theory: Application to Small Molecules and Chromophores *J. Chem. Theor. Comput.* **7** 1344–55

[52] Alberto Castro, Miguel A. L. Marques and Angel Rubio 2004 Propagators for the time-dependent Kohn–Sham equations *J. Chem. Phys.* **121** 3425–33

[53] Magnus W 1954 On the exponential solution of differential equations for a linear operator *Commun. Pure. App. Math.* **7** 649–73

[54] Cheng C-L, Evans J S and Van Voorhis T 2006 Simulating molecular conductance using real-time density functional theory *Phys. Rev. B* **74** 155112

[55] Andreas M. Köster, Jorge M. del Campo, Florian Janetzko and Bernardo Zuniga-Gutierrez 2009 A MinMax self-consistent-field approach for auxiliary density functional theory *J. Chem. Phys.* **130** 114106

[56] Villalobos-Castro J and Köster A M 2021 Diagonalization-free self-consistent field approach with localized molecular orbitals *Theoretical Chemistry Accounts* **140** 152

[57] Kosloff R and Tal-Ezer H 1986 A direct relaxation method for calculating eigenfunctions and eigenvalues of the schrödinger equation on a grid *Chemical Physics Letters* **127** 223–30

[58] Flamant C, Kolesov G, Manousakis E and Kaxiras E 2019 Imaginary-Time Time-Dependent Density Functional Theory and Its Application for Robust Convergence of Electronic States *J. Chem. Theory Comput.* **15** 6036–45

[59] McFarland J and Manousakis E 2020 Imaginary-time time-dependent density functional theory for periodic systems *Journal of Physics: Condensed Matter* **33** 055903

[60] Hekele J, Yao Y, Kanai Y, Blum V and Kratzer P 2021 All-electron real-time and imaginary-time time-dependent density functional theory within a numeric atom-centered basis function framework *J. Chem. Phys.* **155** 154801

[61] Alvarez-Ibarra A, Omar K A, Hasnaoui K and de la Lande A 2022 Chapter 4 Electron and Molecular Dynamics Simulations with Polarizable Embedding *Multiscale Dynamics Simulations: Nano and Nano-bio Systems in Complex Environments* (The Royal Society of Chemistry) pp 117–43

[62] Wu X, Alvarez-Ibarra A, Salahub D R and de la Lande A 2018 Retardation in electron dynamics simulations based on time-dependent density functional theory *Eur. Phys. J. D* **72** 206

[63] Perdew J P, Burke K and Ernzerhof M 1996 Generalized Gradient Approximation Made Simple *Phys. Rev. Lett.* **77** 3865–8

[64] Ross R B, Powers J M, Atashroo T, Ermler W C, LaJohn L A and Christiansen P A 1990 Ab initio relativistic effective potentials with spin–orbit operators. IV. Cs through Rn *J. Chem. Phys.* **93** 6654–70

[65] Pipek J and Mezey P G 1989 A fast intrinsic localization procedure applicable for ab initio and semiempirical linear combination of atomic orbital wave functions *J. Chem. Phys.* **90** 4916–26

[66] de la Lande A, Denisov S and Mostafavi M 2021 The mystery of sub-picosecond charge transfer following irradiation of hydrated uridine monophosphate *Phys. Chem. Chem. Phys.* **23** 21148–62

[67] de la Lande A, Clavaguéra C and Köster A 2017 On the accuracy of population analyses based on fitted densities *J. Mol. Model.* **23** 99

[68] Gill P M W 1994 Molecular integrals Over Gaussian Basis Functions *Advances in Quantum Chemistry* vol 25, ed J R Sabin and M C Zerner (Academic Press) pp 141–205

[69] Obara S and Saika A 1986 Efficient recursive computation of molecular integrals over Cartesian Gaussian functions *J. Chem. Phys.* **84** 3963–74

[70] Calaminici P, Alvarez-Ibarra A, Cruz-Olvera D, Domínguez-Soria V-D, Flores-Moreno R, Gamboa G U, Geudtner G, Goursot A, Mejía-Rodríguez D, Salahub D R, Zuniga-Gutierrez B and Köster A 2016 Auxiliary Density Functional Theory: From Molecules to Nanostructures *Handbook of Computational Chemistry* ed J Leszczynski (Dordrecht: Springer Netherlands) pp 1–67

[71] Dunlap B I, Rösch N and Trickey S B 2010 Variational fitting methods for electronic structure calculations *Mol. Phys.* **108** 3167–80

[72] Mejía-Rodríguez D and Trickey S B 2021 Variational properties of auxiliary density functionals *Theor. Chem. Acc.* **140** 37

[73] Köster A M 2003 Hermite Gaussian auxiliary functions for the variational fitting of the Coulomb potential in density functional methods *J. Chem. Phys.* **118** 9943–51

[74] Köster A M, Reveles J U and del Campo J M 2004 Calculation of exchange-correlation potentials with auxiliary function densities *J. Chem. Phys.* **121** 3417–24

[75] Köster A M, Flores-Moreno R and Reveles J U 2004 Efficient and reliable numerical integration of exchange-correlation energies and potentials *J. Chem. Phys.* **121** 681–90

[76] Lehtola S, Steigemann C, Oliveira M J T and Marques M A L 2018 Recent developments in libxc — A comprehensive library of functionals for density functional theory *SoftwareX* **7** 1–5

[77] Mejía-Rodríguez D and Köster A M 2014 Robust and efficient variational fitting of Fock exchange *J. Chem. Phys.* **141** 124114

[78] Delesma F A, Geudtner G, Mejía-Rodríguez D, Calaminici P and Köster A M 2018 Range-Separated Hybrid Functionals with Variational Fitted Exact Exchange *J. Chem. Theor. Comput.* **14** 5608–16

[79] Tandiana, Rika, Clavaguéra C, Hasnaoui K, Pedroza-Montero, Jesus and de la Lande A 2021 Reliability and Performances of Real-Time Time-Dependent Auxiliary Density Functional Theory Theor. Chem. Acc. **140** *126-138*

[80] Alvarez-Ibarra A, Parise A, Hasnaoui K and de la Lande A 2020 The physical stage of radiolysis of solvated DNA by high-energy-transfer particles: insights from new first principles simulations *Phys. Chem. Chem. Phys.* **22** 7747–58

[81] Flores-Moreno R, Alvarez-Mendez R J, Vela A and Köster A M 2006 Half-numerical evaluation of pseudopotential integrals *Journal of Computational Chemistry* **27** 1009–19

[82] Pedroza-Montero J N, Morales J L, Geudtner G, Álvarez-Ibarra A, Calaminici P and Köster A M 2020 Variational Density Fitting with a Krylov Subspace Method *J. Chem. Theory Comput.* **16** 2965–74

[83] A. Alvarez-Ibarra and A. M. Köster 2013 Double asymptotic expansion of three-center electronic repulsion integrals *J. Chem. Phys.* **139** 024102

[84] Alvarez-Ibarra A and Köster A M 2015 A new mixed self-consistent field procedure *Mol. Phys.* **113** 3128–40

[85] Blackford L S, Choi J, Cleary A J, D'Azevedo E F, Demmel J, Dhillon I S, Dongarra J, Hammarling S, -Henry G, Petitet A, Stanley K, Walker D W and Whaley R C 1997 *ScaLAPACK: A Linear Algebra Library for Message-Passing Computers*

[86] Martínez, Pablo Antonio, Vock, Theresa, Kharchi , Liliane Racha, Pedroza-Montero J N, Hasnaoui K and de la Lande, Aurélien A A Multi-GPU Implementation of Real-Time Time-Dependent Auxiliary Density Functional Theory for the Investigation of Nanosystems Irradiations *Computer Physics Communications* **under review**

[87] Capitani J F, Nalewajski R F and Parr R G 1982 Non-Born-Oppenheimer density functional theory of molecular systems *J. Chem. Phys.* **76** 568–73

[88] Imamura Y, Kiryu H and Nakai H 2007 Colle-Salvetti-type correction for electron-nucleus correlation in the nuclear orbital plus molecular orbital theory *J. Comput. Chem.* **29** 735–40

[89] Udagawa T, Tsuneda T and Tachikawa M 2014 Electron-nucleus correlation functional for multicomponent density-functional theory *Phys. Rev. A* **89** 052519

[90] Brorsen K R, Yang Y and Hammes-Schiffer S 2017 Multicomponent Density Functional Theory: Impact of Nuclear Quantum Effects on Proton Affinities and Geometries *J. Phys. Chem. Lett.* **8** 3488–93

[91] Zubiaga A, Tuomisto F and Puska M J 2014 Full-correlation single-particle positron potentials for a positron and positronium interacting with atoms *Phys. Rev. A* **89** 052707

[92] Goli M and Shahbazian S 2022 Two-component density functional theory for muonic molecules: Inclusion of the electron–positive muon correlation functional *J. Chem. Phys.* **156** 044104

[93] Louisnard F, Mineva T and Cuny J 2022 Impact of nuclear quantum effects on the ^{13}C nuclear shielding of linear carboxylates in water *Theoretical Chemistry Accounts* **141** 36

[94] Li T-C and Tong P 1986 Time-dependent density-functional theory for multicomponent systems *Phys. Rev. A* **34** 529–32

[95] Yang Y, Culpitt T and Hammes-Schiffer S 2018 Multicomponent Time-Dependent Density Functional Theory: Proton and Electron Excitation Energies *J. Phys. Chem. Lett.* **9** 1765–70

[96] Culpitt T, Yang Y, Pavošević F, Tao Z and Hammes-Schiffer S 2019 Enhancing the applicability of multicomponent time-dependent density functional theory *J. Chem. Phys.* **150** 201101

[97] Zhao L, Tao Z, Pavošević F, Wildman A, Hammes-Schiffer S and Li X 2020 Real-Time Time-Dependent Nuclear−Electronic Orbital Approach: Dynamics beyond the Born–Oppenheimer Approximation *J. Phys. Chem. Lett.* **11** 4052–8

[98] Suzuki Y, Hagiwara S and Watanabe K 2018 Time-Dependent Multicomponent Density Functional Theory for Coupled Electron-Positron Dynamics *Phys. Rev. Lett.* **121** 133001

[99] Zhao L, Wildman A, Pavošević F, Tully J C, Hammes-Schiffer S and Li X 2021 Excited State Intramolecular Proton Transfer with Nuclear-Electronic Orbital Ehrenfest Dynamics *J. Phys. Chem. Lett.* **12** 3497–502

[100] Moncada F, Posada E, Flores-Moreno R and Reyes A 2012 Non-Born–Oppenheimer self-consistent field calculations with cubic scaling *Chem. Phys.* **400** 103–7

[101] Mejía-Rodríguez D and de la Lande A 2019 Multicomponent density functional theory with density fitting *J. Chem. Phys.* **150** 174115

[102] Riss U V and Meyer H-D 1995 Reflection-free complex absorbing potentials *Journal of Physics B: Atomic, Molecular and Optical Physics* **28** 1475–93

[103] Pascal Krause, Jason A. Sonk and H. Bernhard Schlegel 2014 Strong field ionization rates simulated with time-dependent configuration interaction and an absorbing potential *J. Chem. Phys.* **140** 174113

[104] Lopata K and Govind N 2013 Near and Above Ionization Electronic Excitations with Non-Hermitian Real-Time Time-Dependent Density Functional Theory *J. Chem. Theor. Comput.* **9** 4939–46

[105] Löwdin P-O 1970 On the Nonorthogonality Problem* *Advances in Quantum Chemistry* vol Volume 5, ed L Per-Olov (Academic Press) pp 185–99

[106] Perdew J P and Levy M 1997 Comment on ``Significance of the highest occupied Kohn-Sham eigenvalue'' *Phys. Rev. B* **56** 16021–8

[107] Delgado J, Lara-Astiaso M, González-Vázquez J, Decleva P, Palacios A and Martín F 2021 Molecular fragmentation as a way to reveal early electron dynamics induced by attosecond pulses *Faraday Discuss.* **228** 349–77

[108] Maitra N T, Burke K and Woodward C 2002 Memory in Time-Dependent Density Functional Theory *Phys. Rev. Lett.* **89** 023002

[109] Fuks J I, Lacombe L, Nielsen S E B and Maitra N T 2018 Exploring non-adiabatic approximations to the exchange–correlation functional of TDDFT *Phys. Chem. Chem. Phys.* **20** 26145–60

[110] Dinh P M, Lacombe L, Reinhard P-G, Suraud É and Vincendon M 2018 On the inclusion of dissipation on top of mean-field approaches *Eur. Phys. J. B* **91** 246

[111] Vignale G 2006 Current Density Functional Theory *Time-Dependent Density Functional Theory* ed M A L Marques, C A Ullrich, F Nogueira, A Rubio, K Burke and E K U Gross (Berlin, Heidelberg: Springer Berlin Heidelberg) pp 75–91

[112] Perdew J P, Parr R G, Levy M and Balduz J L 1982 Density-Functional Theory for Fractional Particle Number: Derivative Discontinuities of the Energy *Phys. Rev. Lett.* **49** 1691–4

[113] Perdew J P and Levy M 1983 Physical Content of the Exact Kohn-Sham Orbital Energies: Band Gaps and Derivative Discontinuities *Phys. Rev. Lett.* **51** 1884–7

[114] Javier Carmona-Espíndola, José L. Gázquez, Alberto Vela and S. B. Trickey 2015 Generalized gradient approximation exchange energy functional with correct asymptotic behavior of the corresponding potential *J. Chem. Phys.* **142** 054105

[115] Carmona-Espíndola J, Gázquez J L, Vela A and Trickey S B 2019 Generalized Gradient Approximation Exchange Energy Functional with Near-Best Semilocal Performance *J. Chem. Theory Comput.* **15** 303–10

[116] Carmona-Espíndola J, Gázquez J L, Vela A and Trickey S B 2020 Negative Electron Affinities and Derivative Discontinuity Contribution from a Generalized Gradient Approximation Exchange Functional *J. Phys. Chem. A* **124** 1334–42

[117] Carmona-Espíndola J, Gázquez J L, Vela A and Trickey S B 2016 Global hybrid exchange energy functional with correct asymptotic behavior of the corresponding potential *Theoretical Chemistry Accounts* **135** 120

[118] Burke K, Werschnik J and Gross E K U 2005 Time-dependent density functional theory: Past, present, and future *J. Chem. Phys.* **123** 062206

[119] Jacquemin D, Perpète E A, Scuseria G E, Ciofini I and Adamo C 2008 TD-DFT Performance for the Visible Absorption Spectra of Organic Dyes: Conventional versus Long-Range Hybrids *J. Chem. Theory Comput.* **4** 123–35

[120] Savin A and Flad H-J 1995 Density functionals for the Yukawa electron-electron interaction *International Journal of Quantum Chemistry* **56** 327–32

[121] Leininger T, Stoll H, Werner H-J and Savin A 1997 Combining long-range configuration interaction with short-range density functionals *Chemical Physics Letters* **275** 151–60

[122] Perdew J P and Zunger A 1981 Self-interaction correction to density-functional approximations for many-electron systems *Phys. Rev. B* **23** 5048–79

[123] Chu S-I 2005 Recent development of self-interaction-free time-dependent density-functional theory for nonperturbative treatment of atomic and molecular multiphoton processes in intense laser fields *J. Chem. Phys.* **123** 062207

[124] Legrand C, Suraud E and Reinhard P-G 2002 Comparison of self-interaction-corrections for metal clusters *Journal of Physics B: Atomic, Molecular and Optical Physics* **35** 1115–28

[125] Ciofini I, Adamo C and Chermette H 2005 Self-interaction error in density functional theory: a mean-field correction for molecules and large systems *Chemical Physics* **309** 67–76

[126] Klüpfel P, Dinh P M, Reinhard P-G and Suraud E 2013 Koopmans' condition in self-interaction-corrected density-functional theory *Phys. Rev. A* **88** 052501

[127] Oliveira M J T, Mignolet B, Kus T, Papadopoulos T A, Remacle F and Verstraete M J 2015 Computational Benchmarking for Ultrafast Electron Dynamics: Wave Function Methods vs Density Functional Theory *J. Chem. Theory Comput.* **11** 2221–33

[128] Kehrer J, Richter R, Foerster J M, Schelter I and Kümmel S 2020 Self-interaction correction, electrostatic, and structural influences on time-dependent density functional theory excitations of bacteriochlorophylls from the light-harvesting complex 2 *J. Chem. Phys.* **153** 144114

[129] Dreuw A and Head-Gordon M 2004 Failure of Time-Dependent Density Functional Theory for Long-Range Charge-Transfer Excited States: The Zincbacteriochlorin−Bacteriochlorin and Bacteriochlorophyll−Spheroidene Complexes *J. Am. Chem. Soc.* **126** 4007–16

[130] Michael J. G. Peach, Peter Benfield, Trygve Helgaker and David J. Tozer 2008 Excitation energies in density functional theory: An evaluation and a diagnostic test *J. Chem. Phys.* **128** 044118

[131] Mulliken R S 1952 Molecular Compounds and their Spectra. II *J. Am. Chem. Soc.* **74** 811–24

[132] Campetella M, Maschietto F, Frisch M J, Scalmani G, Ciofini I and Adamo C 2017 Charge transfer excitations in TDDFT: A ghost-hunter index *Journal of Computational Chemistry* **38** 2151–6

[133] Maschietto F, Campetella M, Sanz García J, Adamo C and Ciofini I 2021 Chasing unphysical TD-DFT excited states in transition metal complexes with a simple diagnostic tool *J. Chem. Phys.* **154** 204102

[134] Le Bahers T, Adamo C and Ciofini I 2011 A Qualitative Index of Spatial Extent in Charge-Transfer Excitations *J. Chem. Theory Comput.* **7** 2498–506

[135] Korsaye F A, de la Lande A and Ciofini I 2022 Following the density evolution using real time density functional theory and density based indexes: Application to model push–pull molecules *Journal of Computational Chemistry* **43** 1464–73

[136] Hirshfeld F L 1977 Bonded-atom fragments for describing molecular charge densities *Theoret. Chim. Acta* **44** 129–38

[137] Becke A D 1988 A multicenter numerical integration scheme for polyatomic molecules *J. Chem. Phys.* **88** 2547–53

[138] A. D. Becke and K. E. Edgecombe 1990 A simple measure of electron localization in atomic and molecular systems *J. Chem. Phys.* **92** 5397–403

[139] Burnus T, Marques M A L and Gross E K U 2005 Time-dependent electron localization function *Phys. Rev. A* **71** 010501

[140] Humphrey W, Dalke A and Schulten K 1996 VMD: Visual molecular dynamics *J. Mol. Graph.* **14** 33–8

[141] Lu T and Chen F 2012 Multiwfn: A multifunctional wavefunction analyzer *Journal of Computational Chemistry* **33** 580–92

[142] Kozlowski D and Pilmé J 2011 New insights in quantum chemical topology studies using numerical grid-based analyses *J. Comput. Chem.* **32** 3207–17

[143] Silvi B and Savin A 1994 Classification of chemical bonds based on topological analysis of electron localization functions *Nature* **371** 683

[144] Piquemal J P, Pilmé J, Parisel O, Gérard H, Fourré I, Bergès J, Gourlaouen C, de La Lande A, Van Severen M C and Silvi B 2008 What can be learnt on biologically relevant systems from the topological analysis of the electron localization function? *Int. J. Quantum Chem* **108** 1951–69

[145] Pilmé J, Luppi E, Bergès J, Houée-Lévin C and de la Lande A 2014 Topological analyses of time-dependent electronic structures: application to electron-transfers in methionine enkephalin *J. Mol. Model.* **20** 2368

[146] Parise A, Alvarez-Ibarra A, Wu X, Zhao X, Pilmé J and de la Lande A 2018 Quantum Chemical Topology of the Electron Localization Function in the Field of Attosecond Electron Dynamics *J. Phys. Chem. Lett.* 844–50

[147] Gamboa G U, Calaminici P, Geudtner G and Köster A M 2008 How Important are Temperature Effects for Cluster Polarizabilities? *J. Phys. Chem. A* **112** 11969–71

[148] Calaminici P, Köster A M and Martinez G U G 2007 Temperature Dependence of the Polarizability of Sodium Clusters: An all-electron Density Functional Study *AIP Conference Proceedings* **963** 207–11

[149] Verma P, Ghosh D and Dutta A K 2021 Electron Attachment to Cytosine: The Role of Water *J. Phys. Chem. A* **125** 4683–94

[150] Anstöter C S, DelloStritto M, Klein M L and Matsika S 2021 Modeling the Ultrafast Electron Attachment Dynamics of Solvated Uracil *J. Phys. Chem. A* **125** 6995–7003

[151] Kohanoff J, McAllister M, Tribello G and Gu B 2017 Interactions between low energy electrons and DNA: a perspective from first-principles simulations *J. Phys.: Condens. Matter* **29** 383001

[152] Feng W-L and Tian S X 2015 Ab Initio Molecular Dynamics Simulation Study of Dissociative Electron Attachment to Dialanine Conformers *J. Phys. Chem. A* **119** 1838–45

[153] MCKIBBEN J M 1984 Chemistty of the Purex Process **36** 3–16

[154] Mincher B J, Modolo G and Mezyk S P 2009 Review Article: The Effects of Radiation Chemistry on Solvent Extraction: 1. Conditions in Acidic Solution and a Review of TBP Radiolysis *Solvent Extr. Ion Exch.* **27** 1–25

[155] Řezáč J, Lévy B, Demachy I and de la Lande A 2012 Robust and Efficient Constrained DFT Molecular Dynamics Approach for Biochemical Modeling *J. Chem. Theor. Comput.* **8** 418–27

[156] Ma J, Denisov S A, Marignier J-L, Pernot P, Adhikary A, Seki S and Mostafavi M 2018 Ultrafast Electron Attachment and Hole Transfer Following Ionizing Radiation of Aqueous Uridine Monophosphate *J. Phys. Chem. Lett.* **9** 5105–9

[157] Tavernelli I, Röhrig U F and Rothlisberger U 2005 Molecular dynamics in electronically excited states using time-dependent density functional theory *Mol. Phys.* **103** 963–81

[158] Li X, Tully J C, Schlegel H B and Frisch M J 2005 Ab initio Ehrenfest dynamics *J. Chem. Phys.* **123** 084106

[159] Kirrander A and Vacher M 2020 Ehrenfest Methods for Electron and Nuclear Dynamics *Quantum Chemistry and Dynamics of Excited States* pp 469–97

[160] Craig C F, Duncan W R and Prezhdo O V 2005 Trajectory Surface Hopping in the Time-Dependent Kohn-Sham Approach for Electron-Nuclear Dynamics *Phys. Rev. Lett.* **95** 163001

[161] de la Lande A, Alvarez-Ibarra A, Hasnaoui K, Cailliez F, Wu X, Mineva T, Cuny J, Calaminici P, López-Sosa L, Geudtner G, Navizet I, Garcia Iriepa C, Salahub D R and Köster A M 2019 Molecular Simulations with in-deMon2k QM/MM, a Tutorial-Review *Molecules* **24** 1653

[162] Warshel A and Levitt M 1976 Theoretical studies of enzymic reactions: Dielectric, electrostatic and steric stabilization of the carbonium ion in the reaction of lysozyme *J. Mol. Biol.* **103** 227–49

[163] Ramachandran K I, Gopakumar D and Namboori K 2008 Semiempirical Methods *Computational Chemistry and Molecular Modeling: Principles and Applications* (Berlin, Heidelberg: Springer Berlin Heidelberg) pp 139–54

[164] Vanommeslaeghe K, Guvench O and Jr. D M A 2014 Molecular Mechanics *Current Pharmaceutical Design* **20** 3281–92

[165] Kubař T, Welke K and Groenhof G 2015 New QM/MM implementation of the DFTB3 method in the gromacs package *Journal of Computational Chemistry* **36** 1978–89

[166] Sanz-Navarro C F, Grima R, García A, Bea E A, Soba A, Cela J M and Ordejón P 2011 An efficient implementation of a QM–MM method in SIESTA *Theoretical Chemistry Accounts* **128** 825–33

[167] Zalevsky A O, Reshetnikov R V and Golovin A V 2018 New QM/MM Implementation of the MOPAC2012 in the GROMACS *RuSCDays*

[168] Salahub D, Noskov S, Lev B, Zhang R, Ngo V, Goursot A, Calaminici P, Köster A, Alvarez-Ibarra A, Mejía-Rodríguez D, Řezáč J, Cailliez F and de la Lande A 2015 QM/MM Calculations with deMon2k *Molecules* **20** 4780

[169] Field M J, Bash P A and Karplus M 1990 A combined quantum mechanical and molecular mechanical potential for molecular dynamics simulations *J. Comput. Chem.* **11** 700–33

[170] Jorgensen W L, Maxwell D S and Tirado-Rives J 1996 Development and Testing of the OPLS All-Atom Force Field on Conformational Energetics and Properties of Organic Liquids *J. Am. Chem. Soc.* **118** 11225–36

[171] Salomon-Ferrer R, Case D A and Walker R C 2013 An overview of the Amber biomolecular simulation package *Wiley Interdisciplinary Reviews: Computational Molecular Science* **3** 198–210

[172] Mineva T and Russo N 1997 Solvent effects computed with the Gaussian density functional method *Int. J. Quantum Chem* **61** 665–71

[173] B. R. Brooks, C. L. Brooks III, A. D. Mackerell Jr, L. Nilsson, R. J. Petrella, B. Roux, Y. Won, G. Archontis, C. Bartels, S. Boresch, A. Caflisch, L. Caves, Q. Cui, A. R. Dinner, M. Feig, S. Fischer, J. Gao, M. Hodoscek, W. Im, K. Kuczera, T. Lazaridis, J. Ma, V. Ovchinnikov, E. Paci, R. W. Pastor, C. B. Post, J. Z. Pu, M. Schaefer, B. Tidor, R. M. Venable, H. L. Woodcock, X. Wu, W. Yang, D. M. York and M. Karplus 2009 CHARMM: The biomolecular simulation program *J. Comput. Chem.* **30** 1545–614

[174] Lagardere L, Jolly L-H, Lipparini F, Aviat F, Stamm B, Jing Z F, Harger M, Torabifard H, Cisneros G A, Schnieders M J, Gresh N, Maday Y, Ren P Y, Ponder J W and Piquemal J-P 2018 Tinker-HP: a massively parallel molecular dynamics package for multiscale simulations of large complex systems with advanced point dipole polarizable force fields *Chem. Sci.* **9** 956–72

[175] Abraham M J, Murtola T, Schulz R, Páll S, Smith J C, Hess B and Lindahl E 2015 GROMACS: High performance molecular simulations through multi-level parallelism from laptops to supercomputers *SoftwareX* **1–2** 19–25

[176] Samaniego-Rojas J D, Hernández-Segura L-I, López-Sosa L, Delgado-Venegas R I, Gomez B, Lambry J-C, de la Lande A, Mineva T, Alejandre J, Zúñiga-Gutiérrez B A, Flores-Moreno R, Calaminici P, Geudtner G and Köster A M 2022 Chapter 1 QM/MM with Auxiliary DFT in deMon2k *Multiscale Dynamics Simulations: Nano and Nano-bio Systems in Complex Environments* (The Royal Society of Chemistry) pp 1–54

[177] Ziegler J F 1999 Stopping of energetic light ions in elemental matter *Journal of Applied Physics* **85** 1249–72

[178] Warshel A, Kato M and Pisliakov A V 2007 Polarizable Force Fields: History, Test Cases, and Prospects *J. Chem. Theor. Comput.* **3** 2034–45

[179] Wu X 2018 *Contribution to the Development of Advanced Approaches for Electron and Molecular Dynamics Simulations in Extended Biomolecules* Theses (Université Paris Saclay (COmUE))

[180] Wu X, Teuler J-M, Cailliez F, Clavaguéra C, Salahub D R and de la Lande A 2017 Simulating Electron Dynamics in Polarizable Environments *J. Chem. Theor. Comput.* **13** 3985–4002

[181] de la Lande A 2021 Femtosecond responses of hydrated DNA irradiated by ionizing rays focus on the sugar-phosphate part *Theoretical Chemistry Accounts* **140** 77

[182] Wang Z-X, Zhang W, Wu C, Lei H, Cieplak P and Duan Y 2006 Strike a balance: Optimization of backbone torsion parameters of AMBER polarizable force field for simulations of proteins and peptides *J. Comput. Chem.* **27** 781–90